

DEGREE PROJECT IN VEHICLE ENGINEERING
SECOND CYCLE, 30 CREDITS
STOCKHOLM, SWEDEN 2025



Study on train driving strategies in virtual coupling operation

DANLIN FANG





Study on train driving strategies in virtual coupling operation

DANLIN FANG

Master's Programme, Vehicle Engineer

Supervisor: William Z. Liu

Examiner: Sebastian Stichel

MSc in Vehicle Engineering, School of Engineering Sciences

Swedish title: Strategier för att köra virtuellt kopplade tåg

Date: 2025-12-05

Abstract

Virtual coupling (VC) is a promising train operation concept that uses train-to-train communication and cooperative control to enable short inter-train spacing and increase line capacity without major infrastructure upgrades. Its application to heavy-haul railways, however, remains challenging because of long train formations, complex track conditions, large system inertia, and strict safety requirements. This thesis therefore investigates driving strategies for heavy-haul trains operating under virtual coupling.

A longitudinal simulation framework is developed for a two-train leader–follower scenario. Based on a single-point dynamics model, a multi-point treatment of track inputs is introduced to account for train-length effects through equivalent gradient and equivalent curve radius. Communication delay and actuation delay are included, and a predictive safety layer is incorporated to constrain the admissible acceleration near the safety limit. On this basis, a velocity-based artificial potential field (APF) control strategy is proposed, and the control demand is mapped to traction, regenerative braking, and mechanical braking commands.

Simulation results based on the LKAB heavy-haul line and IORE train data show that the proposed method can reproduce the key longitudinal operating characteristics of heavy-haul virtual coupling and maintain safe and stable train following during start-up, cruising, stopping, and restart. Compared with conventional feedback control, the APF-based strategy provides smoother following behaviour, better suppression of speed oscillations, and improved spacing stability. The parameter study further indicates that a start-up delay of 30–60 s, an acceleration constraint of ± 0.3 m/s², and an initial/target spacing of around 200 m lead to favourable overall operating performance.

Keywords

Virtual coupling, Heavy-haul train, Driving strategy, Cooperative control, Artificial potential field, Longitudinal train dynamics

Sammanfattning

Virtuell koppling (VC) är ett lovande koncept för tågdrift som använder kommunikation mellan tåg och samverkande styrning för att möjliggöra korta avstånd mellan tåg och öka linjekapaciteten utan större uppgraderingar av infrastrukturen. Tillämpningen på järnvägar för tung godstrafik är dock fortfarande utmanande på grund av långa tågsätt, komplexa spårförhållanden, stor systemtröghet och strikta säkerhetskrav. Denna avhandling undersöker därför körstrategier för tunga godståg som framförs under virtuell koppling.

Ett longitudinellt simuleringsramverk utvecklas för ett scenario med två tåg i en leader–follower-konfiguration. Med utgångspunkt i en enpunktsmodell för tågdynamik införs en flerpunktsbehandling av spårindata för att ta hänsyn till tåglängdens inverkan genom ekvivalent lutning och ekvivalent kurvradie. Kommunikationsfördröjning och aktueringsfördröjning inkluderas, och ett prediktivt säkerhetslager införs för att begränsa den tillåtna accelerationen nära säkerhetsgränsen. På denna grund föreslås en hastighetsbaserad styrstrategi baserad på artificiellt potentialfält (APF), och styrsignalen mappas vidare till kommandon för dragkraft, regenerativ bromsning och mekanisk bromsning.

Simuleringsresultat baserade på data från LKAB:s bana för tung godstrafik och IORE-tåg visar att den föreslagna metoden kan återge de viktigaste longitudinella driftegenskaperna hos virtuell koppling för tung godstrafik och upprätthålla säker och stabil tågföljning vid igångkörning, färd i konstant hastighet, stopp och återstart. Jämfört med konventionell återkopplingsstyrning ger den APF-baserade strategin jämnare tågföljning, bättre dämpning av hastighetsoscillationer och förbättrad stabilitet i tågavståndet. Parameterstudien visar vidare att en startfördröjning på 30–60 s, en accelerationsbegränsning på $\pm 0.3 \text{ m/s}^2$ och ett initialt/målsatt tågavstånd på omkring 200 m ger gynnsam total driftprestanda.

Keywords

Virtuell koppling, Tungt godståg, Körstrategi, Samverkande styrning, Artificiellt potentialfält, Longitudinell tågdynamik

Acknowledgements

In 2024, I came to KTH and started a new stage of my studies. During my undergraduate studies, my academic background was mainly in vehicle engineering with a focus on the automotive field. My study experience at Beijing Jiaotong University gradually introduced me to the railway field and deepened my interest in it. This was also one of the main reasons why I eventually chose this research topic.

The completion of this thesis marks the end of this stage of my studies at KTH. Throughout the research and writing process, I received support and help from many teachers, classmates, friends, and family members. Here, I would like to express my sincere gratitude to everyone who has cared for, supported, and helped me.

First of all, I would like to sincerely thank my supervisor, William Z. Liu, for his valuable advice, patient guidance, and in-depth discussions throughout this research. His support has benefited me greatly and helped me overcome many of the difficulties and challenges along the way.

I would also like to thank Sebastian Stichel, the coordinator of the dual master's programme, for giving me the valuable opportunity to study at KTH and for serving as the examiner of this thesis. I truly appreciate his guidance and support during both the research and examination process.

My sincere thanks also go to Beijing Jiaotong University and the China Scholarship Council for their financial support for my exchange studies, which enabled me to successfully complete my study and research at KTH.

Finally, I would like to thank my parents for their constant love and support, which have always been an important source of strength for me.

December 2025
Danlin Fang

CONTENTS

1	Introduction	1
1.1	Background.....	1
1.2	Purpose	3
1.3	Goals	4
1.4	Delimitations.....	4
1.5	Structure of the thesis	5
2	Literature Review.....	6
2.1	Virtual coupling in railway system.....	6
2.2	Train safety tracking mode	9
2.3	Dynamic inter-train spacing in virtual coupling.....	13
2.4	Control architecture in virtual coupling.....	17
2.5	Control methods for virtual coupling driving strategies	21
2.6	Summary.....	23
3	Methodology	25
3.1	Overview of Research Framework.....	25
3.2	Simulation Tool	28
3.3	Data Collection	29
3.4	Key performance indicators (KPIs).....	30
4	Modelling.....	32
4.1	Multi-point train modelling.....	33
4.1.1	Equivalent curve radius processing	33
4.1.2	Equivalent gradient processing	35
4.2	Dynamic modelling.....	37
4.2.1	Model assumption.....	37
4.2.2	Dynamic model assumption.....	37
4.2.3	Traction force calculation.....	38
4.2.4	Braking force calculation.....	38
4.2.5	Running resistance calculation	39
4.2.6	Gradient resistance calculation	40
4.2.7	Curve resistance calculation.....	41

4.3	Time-domain treatment.....	41
4.4	Communication and actuation delay processing	43
4.5	Two-train cooperative control model	46
4.5.1	Preprocessing rules.....	46
4.5.2	Finite-horizon inter-train spacing prediction model.....	49
4.5.3	Predictive safety control mechanism	51
4.5.4	Velocity-based artificial potential field control	52
4.5.5	Stopping and restart control	56
4.6	Case study setup and description	61
4.6.1	Train	61
4.6.2	Track.....	62
4.6.3	Representative simulation scenario and control activation timeline.....	64
4.7	Summary.....	67
5	Results and discussion	70
5.1	Comparative analysis of the single-point model and multi-point model	70
5.2	Impact of the proposed driving strategy on train operation.....	72
5.3	Effects of different control function formulations on train operation.....	74
5.4	Comparison of distance-based and speed-based driving strategies.....	78
5.5	Optimization and sensitivity analysis of driving strategy parameters	81
5.5.1	Influence of start-delay settings.....	81
5.5.2	Influence of acceleration limits	84
5.5.3	Effects of initial and target inter-train spacing settings.....	87
5.6	Summary.....	91
6	Conclusions and future work.....	92
6.1	Conclusions.....	92
6.2	Future work.....	93
	References.....	95

1 Introduction

1.1 Background

Rail transport plays a central role in modern integrated transport systems for long-distance, high-volume freight. In particular, it provides large capacity, low cost, and reliable services for the long-term and stable movement of commodities such as ore and coal, which are difficult to replace with road or waterway transport. For heavy-haul corridors that primarily serve goods export, transport capacity on existing infrastructure has become a key bottleneck for regional logistics efficiency and industrial development. Therefore, studying the operating characteristics and control methods of heavy-haul trains to increase capacity is of clear engineering relevance and practical importance.

Compared with passenger trains, heavy-haul trains are generally longer and heavier, and have more complex operating environments. They are highly sensitive to gradients, curve radius, aerodynamic drag, and available traction. Any speed variation is amplified by the large mass, leading to long braking distances, large longitudinal force impacts, less room for corrective control action, and greater control difficulty than short freight or passenger trains. At the same time, heavy-haul lines often traverse mining areas, mountainous regions, or coastal zones, where steep gradients, dense curves, and adverse weather are common. As a result, train spacing typically requires a large safety margin, which further restricts the usable line capacity.

To cope with increasing transport demand, railway operators have attempted to enhance capacity on several levels. On the infrastructure side, they build or densify lines, add sidings, and expand stations. On the train side, they extend train length and increase axle load and operating speed. On the operations side, they optimize timetables, improve dispatching, and apply flexible marshalling. On the signaling and control side, they have evolved from fixed-block to moving-block systems (such as CBTC and ERTMS Level 3) in order to shorten the protection spacing between trains. Although these measures have eased capacity pressure to some extent, factors such as investment cost, construction time, line conditions, and safety margins mean that many of them are now approaching their physical or economic limits. As a result, there is limited room for further improvement if one relies only on traditional approaches.

Thanks to the development of communication and automatic control technologies, the train operation modes can be further optimized. For instance, with the improvement of train-to-train (T2T) communication capabilities, trains can share key information such as speed, acceleration, and traction/braking commands in real time, thus the following trains can actively adjust their behavior based on the actual operating states of the leader train. This is what we call Virtual Coupling (VC), a new operation mode that differs from the traditional mechanical coupling. Specifically, this mode can make the train group behave like one long train without physical coupler connections. This new mode has the potential to significantly reduce train inter-train spacings and enhance line capacity with little or no additional infrastructure, thereby providing a breakthrough technical pathway for enhancing heavy-haul railway capacity.

However, VC still faces numerous challenges, including strong dependence of safety on T2T communication, complex signaling and cyber-security architectures, and difficulties in coordinating heterogeneous trains. Existing research mainly focuses on communication architectures, signaling systems, and control-algorithm design. Less attention has been paid to the following question in the heavy-haul train scenario: how to apply VC in the train operation mode and realize longitudinal train control from the perspective of

automated driving strategies (coordinated traction/braking control), so that the inter-train spacing is constrained while ensuring operational safety, and thus supporting higher line capacity for a train group.

Based on this, this thesis focuses on VC operation of heavy-haul trains. It systematically studies longitudinal train dynamics modeling, cooperative control, and automated driving strategies, and conducts simulations under real line conditions, aiming to provide theoretical and methodological support for improving line capacity of next-generation heavy-haul railways.

1.2 Purpose

This study focuses on train control under VC operation. The core objective is to develop driving strategies for multi-train cooperative operation, based on a combination of train operating behavior, driving mode, and line characteristics. Under this overall objective, the main work can be summarized as follows.

First, this study hopes to provide new technical ideas and methods support for railway transportation through the discussion of the VC operation mode. As we know, VC depends not only on communication and the control system, but also on line gradients, curvature, and braking performance. Therefore, from a driving strategy view, this thesis proposes a cooperative control method and tests it with simulations on typical line conditions. The simulations use real-line gradients, curves, and operating conditions, so the strategy is closer to practice and can support future engineering implementation.

Second, VC reduces the inter-train spacing, so the driving strategy has to be more accurate and robust. Based on longitudinal train dynamics, this thesis studies how speed difference, acceleration difference, and gradient disturbances affect cooperative operation in a train group. It then explores stable and safe traction/braking force regulations to achieve steadier following control between the leader train and the following train. This helps to explain how the VC system works and provides a basis for future dispatch optimization and control algorithm improvement.

Finally, this work also supports the author's learning goals. Through these dynamics modeling, control design, and simulation validation, the author builds skills in vehicle dynamic modeling, automated control strategy development, and data analysis. These experiences broaden research understanding and lay a foundation for future engineering and research work.

1.3 Goals

To achieve the research aims outlined above, this study sets out the following specific objectives:

- To review the current state of research on cooperative operation and driving strategies for virtual coupling trains.
- To build a multi-point model for train longitudinal dynamics that explicitly accounts for train length.
- To develop a train dynamics model suitable for virtual coupling scenarios.
- To design cooperative control strategies tailored to the operating characteristics of virtual coupling.
- To build a simulation environment based on real track information to validate the proposed control strategies.
- To summarise the performance of the control strategies under different track conditions and operating scenarios.

These objectives together form the core of this study. The dynamics models and control strategies are the basis for VC operation, and simulation studies based on real line data are an important step to verify the effectiveness of the proposed methods. By completing these tasks, it aims to support further application of VC in freight railways, and also reflects the author's professional capability in both engineering practice and academic research.

1.4 Delimitations

The scope of this study is mainly the longitudinal operating behavior of trains, with a focus on speed, acceleration, and inter-train spacing. The dynamics are

modeled using a multi-point model. It accounts for the effect of train length on how gradient and curvature inputs vary along the train, but it does not consider lateral dynamics, vehicle vibration, or aerodynamic coupling.

For the control strategy, this study focuses on short inter-train spacing cooperative operation, including the following logic between the trains, safety constraints, and coordinated traction/braking control. It does not address engineering details such as train control system architecture, communication protocol implementation, or hardware deployment. Communication delay and errors are represented by typical parameter values, rather than a full communication system model.

The simulation environment is built from real-line gradients, curve radius, and speed-limit data. The goal is to examine the dynamic behavior and feasibility of the proposed strategy, not to fully simulate all real-world operating states. The current work only considers two-train coupling; cases with three or more trains in a train group require further study. In addition, there is no experimental validation yet, such as hardware-in-the-loop, virtual demonstration, and field tests are still needed.

1.5 Structure of the thesis

The structure of the remaining chapters in this thesis follows the research objectives outlined in this chapter. Chapter 2 reviews the research progress on virtual coupling and related fields, then summarizes the main features and limitations of existing approaches. Chapter 3 presents the overall framework adopted in this study, together with the simulation tools and data-preparation process. Chapter 4 focuses on the methods for train dynamics modelling, track data processing, communication-delay handling, and the construction of cooperative control strategies, and also describes the case-study setup. Chapter 5 presents the simulation results and analyses how different models, control strategies, and parameter settings affect train operating performance. Chapter 6 summarizes the work conducted in this thesis and outlines directions for future research.

2 Literature Review

2.1 Virtual coupling in railway system

The core topic of this thesis is Virtual Coupling (VC), so we first review the development of it.

The idea of VC can be traced back to the concept of “virtually coupled train formations” proposed by Bock and Varchmin in 1999 [1]. Rather than just improving the existing train control, they described a new operation mode between highway vehicle formation and traditional railway formation. In this mode, trains run continuously as a “fleet”. Each train has its own traction and braking system, and the formation is logically coupled through continuous regulation of speed and inter-train spacing. This approach can reduce the spacing to nearly the mechanical coupling effect, significantly enhancing the line utilization and line capacity [1]. In addition, they proposed to realize the operation mode of non-fixed block partition by dynamically calculating the braking distance and safety distance, which can be regarded as the early prototype of the subsequent concept of relative braking and moving block.

Based on this, Braun, König and Schnieder extended the research from the operational aspect to the system engineering level, and proposed the overall architecture of the “Future Railway Management System(RMS)” [2]. They

pointed out that the existing management structure is mainly based on centralized scheduling. This structure cannot adequately support the high-density and dynamic operational requirements of VC. Therefore, some functions such as train path allocation, priority coordination and conflict resolution should be jointly undertaken by the distributed information system and the multi-agent mechanism [2]. Following this idea, some studies have constructed workable control frameworks for virtual-coupled fleets in the simulation, which makes VC technology gradually progress from abstract concept to evaluable operation scheme. However, these simulations mainly focused on freight scenarios, and it is necessary to assume that the communication and positioning capabilities are extremely ideal [3].

Henke et al. further carried out physical verification work. They constructed an autonomous train fleet on a 1:2.5 scale test line, and realized the dynamic coupling and decoupling of the train during operation through fleet communication and formation control [4]. Their experiments were the first time to show the physical feasibility under the condition without mechanical connection, but due to the limitation of platform scale and scene complexity, they did not cover the many disturbances seen in real operations. At the same time, Ständer et al. also defined “virtual train-sets” from the perspective of safety and train operation mode, and set out the corresponding safety concept model [5].

So, early studies have basically outlined the main characteristics of VC: no physical coupling, relying on high-precision positioning and train-to-train/train-to-ground communication, and organizing the fleet with short inter-train spacing under the relative braking distance framework. But at that time, due to the limitations of communication, positioning and computing capabilities, most work stayed in the stage of freight application, small-scale tests or idealized simulation verification, and lacked deep integration with mainstream signaling systems such as ERTMS/ETCS [6,7].

After that, the European Union Shift2Rail program and its subsequent Europe's Rail joint venture made VC a rapid development. Shift2Rail has listed VC as

one of the key research directions, and set up many projects in moving block, train-to-train communication, and train autonomous operation [6]. Gkoumas et al. also found that VC has been regarded as a key innovation to improve capacity, flexibility and network resilience [6].

Current research has proved the development potential of VC from various perspectives once again. From the view of operational safety, Ständer et al. pointed out that if communication is reliable and control logic is guaranteed, VC can reach at least the same safety standard as traditional control systems [5], indicating that cancelling the physical linkages will not weaken the safety. For capacity evaluation, Flammini et al. used a Petri net model to quantify VC operation. The results show that compared with the conventional blocking mode, VC can bring higher line capacity and more stable throughput performance under various working conditions [8]. Di Meo et al. then carried out numerical simulations within the ERTMS/ETCS framework to further confirm the potential benefits of VC in capacity improvement, response speed and operating efficiency [9]. These confirmed advantages provide a solid basis and motivation for further development of VC.

Through the review above, it can be seen that most research focuses on the cooperative control design of control algorithm and system level, such as model predictive control, robust control, cooperative control, distributed control and vehicle-following model, as shown in Figure 2.1 [7]. Such studies generally assume that trains follow a given speed profile, and the function to generate acceleration is often encapsulated within the controller as an “execution layer” process. More specifically, the real-time allocation of traction and braking forces is usually not treated as an independent decision variable.

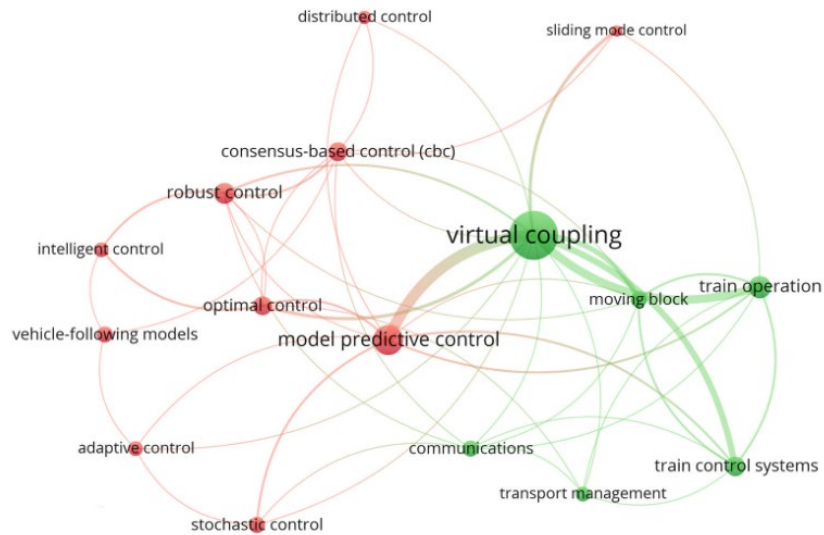


Figure 2.1 Main research topics identification [7]

In traditional train control systems, this assumption is usually acceptable. But in VC, without physical coupling, the following train maintains the inter-train spacing mainly by updating traction and braking commands in real time based on the leader train’s state. So, the traction and braking distribution at the driving-strategy level acts as a dynamic distance regulator. But few studies take this operational view and systematically explore how to adjust the traction or braking level (or percentage) using line gradients, curves, speed-limit points, stop points, and the leader train’s operating state to satisfy the required safety distance. Therefore, developing a driving strategy that can adjust traction and braking force distribution in real time is important for improving both the safety and efficiency of VC operation.

2.2 Train safety tracking mode

Throughout the development of railway transportation, how to maintain the safety distance between trains has always been one of the most crucial issues, which results in the forming of the train block systems. Here, “block” refers to a way of occupation management of the track section. This system ensures that only one train can enter a certain section at the same time, and utilizes this spatial isolation to ensure that trains will not collide. Current tracking modes mainly include the fixed block system, quasi-moving block system, moving block system, and virtual coupling.

Among them, the most widely used and most mature one is the Fixed Block System (FBS), and it was also the first to be developed. It divides a line into block sections of equal length, and trains must run in turn according to those blocks. To further improve safety, the system usually sets up an additional protection section, so that the following train can have a sufficient buffer distance before entering the area occupied by the leader train. This structure is indeed safe, but because of the fixed block length, the inter-train spacing is largely fixed as well, so line capacity is limited to some extent.

Among FBS, the main types are manual block system, semi-automatic block system, and automatic block system, and the fixed automatic block system is the most widely used one [10]. This system uses track circuits to detect train positions in real time. It then combines this information with block occupancy information and signal displays to determine whether movement authority can be granted to the train. In this mode, generally only one train is allowed to occupy each section. But in some sections with clear one-way operation, multiple trains can be permitted to enter in sequence through different signal displays, so the system can improve efficiency to some extent.

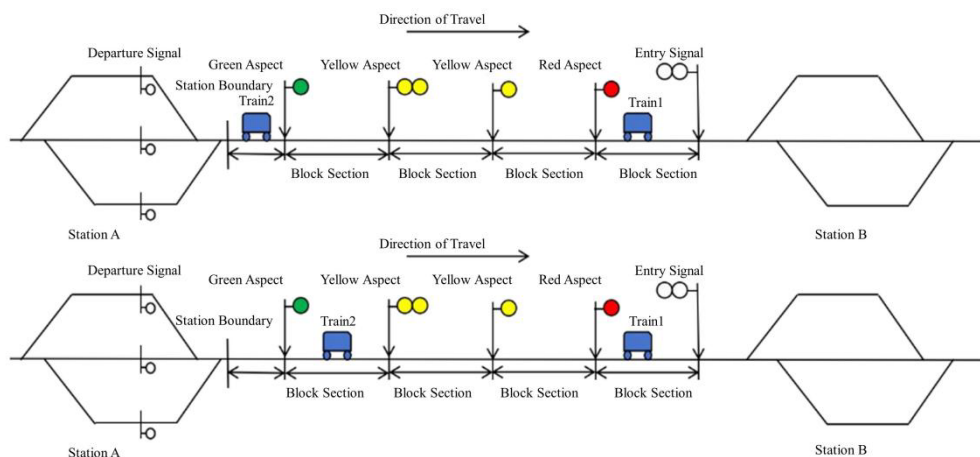


Figure 2.2 Schematic diagram of a four-aspect fixed block system

Later, the quasi-moving block system is proposed as a transitional scheme. It allows the following train to start braking closer to the leader train, as long as it can ensure a safe stop in the end. More specifically, the target braking point for the following train is set at the start of the block section currently occupied by the leader train, with just a certain safety distance reserved, so that the inter-

train spacing can be shortened, and the usage efficiency of the line can also be improved. However, since the following train cannot stop within the block occupied by the leader train, this approach still inherits the structural constraints of fixed block sections.

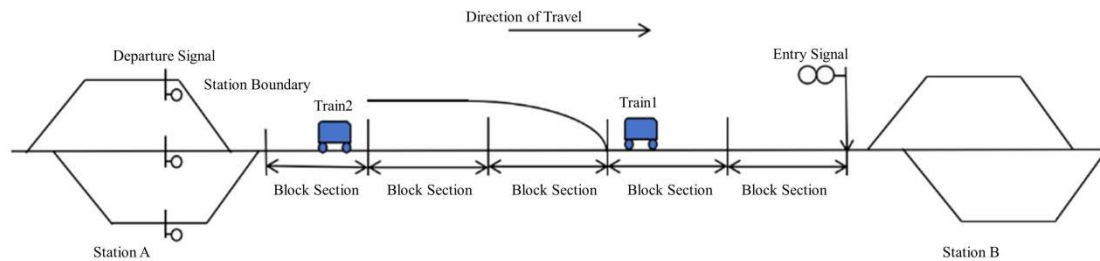


Figure 2.3 Schematic Diagram of a Quasi-Moving Block System

Next, the Moving Block System (MBS) appeared, which successfully broke through the limitations of fixed blocks, as shown in Figure 2.4. In such systems, the leader train continuously calculates and reports its own position and speed, and the ground control center will calculate the safe braking distance in real time and distribute the allowable operating envelope range to the following train. Compared with FBS, since the safety distance of MBS changes continuously over time, the following train can run closer to the leader train while still meeting the braking safety requirements, thus significantly shortening the inter-train spacing and improving the line capacity [11]. This can also be considered as the basic idea of the next VC technology.

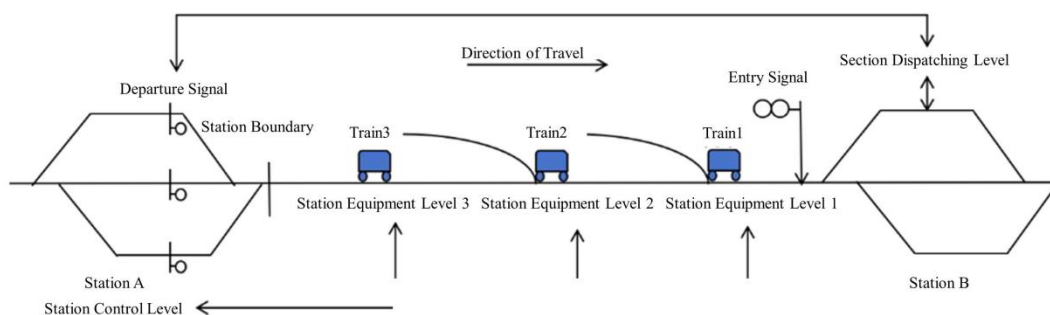


Figure 2.4 Schematic Diagram of the Moving Block System Principle

MBS can be divided into two types based on the calculation method: absolute moving block and relative moving block. They are also often described as the “hard-wall” and “soft-wall” modes. The difference between them is that the former only considers the current position of the leader train when calculating

the safety distance, and regards the leader train as a stationary obstacle, so that the running boundary of the following train is the “hard wall”. The latter incorporates dynamic information such as the speed and deceleration of the leader train into the calculation. When the leader train brakes, the following train needs to brake in advance to decelerate based on the movement trend of the leader train [12]. Because of making full use of the dynamic information of the leader train, the latter can further shorten the inter-train spacing and further improve the capacity of the line.

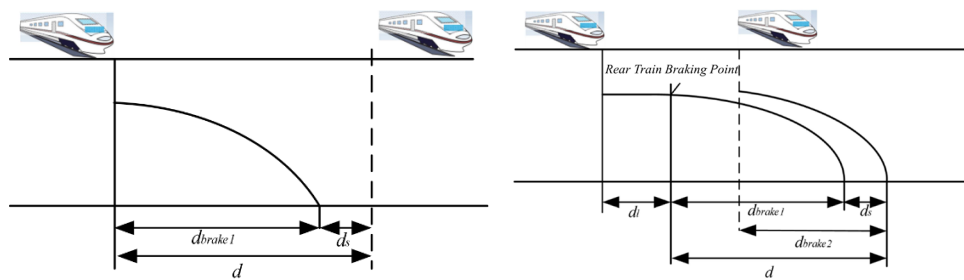


Figure 2.5 Speed-distance curve of two moving block mode

Figure 2.5 is a comparison of the speed-distance curves of the two modes, where d is the minimum inter-train spacing, d_s is the safety distance, d_{brake1} and d_{brake2} represent the braking distances of the two trains, and d_1 represents the shortened distance after the method improvement.

All of these modes essentially aim to compress the inter-train spacing as much as possible under the safety constraints, in order to improve the line capacity. VC goes one step further on the basis of relative moving block: trains are no longer treated as independent tracking units, but are organized into a virtual train group. The following train can use real-time information from the leader train to continuously adjust its traction and braking commands, maintaining a compact yet safe inter-train spacing. It also allows trains within the group to be coupled or decoupled as needed. This new mode offers a technical path to exploit existing line capacity and improve operational flexibility without major infrastructure upgrades.

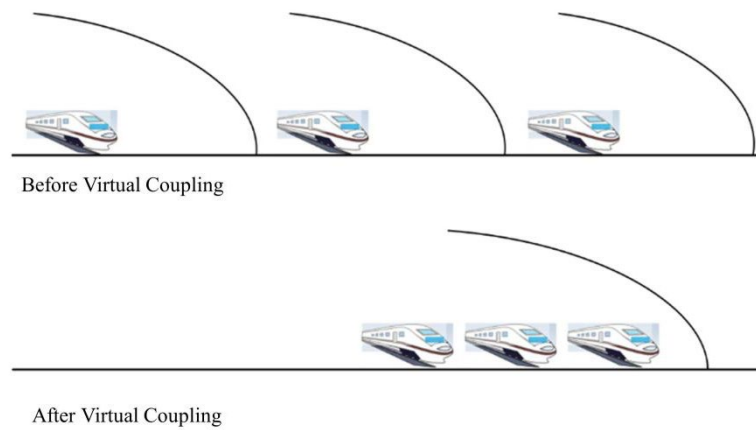


Figure 2.6 Comparison before and after virtual coupling

2.3 Dynamic inter-train spacing in virtual coupling

In VC, dynamic inter-train spacing refers to the real-time distance between the following train and the leader train during train-following, and it is a key parameter affecting operation safety and capacity. It is not only limited by the speed, acceleration and braking performance of two trains, but also affected by communication delay, position accuracy and operation fluctuation.

Before performing the calculations, the safety braking model is introduced, which provides the essential basis for constructing dynamic inter-train spacing and operational constraints. According to the common performance requirements of the IEEE for the CBTC system, the train does not immediately enter the stable deceleration stage after the emergency braking, but undergoes a series of processes. The researchers found that this process is usually divided into the following stages: equipment response stage, traction interruption stage, constant speed stage, braking establishment stage and final braking stage, as shown in Figure 2.7 [13].

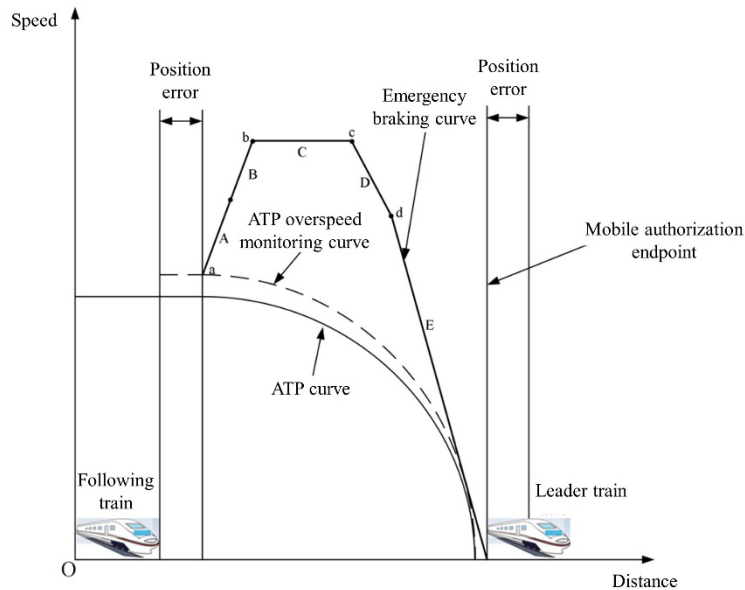


Figure 2.7 Typical safety braking model

In the equipment response stage (stage A), the following train is still under traction, and there is a response delay between receiving the braking command and the start of traction cut-off. Its duration is related to the system processing time $t_r + t_m$, where t_r is the response time of the train control unit and t_m is the mechanism delay in braking message transmission and actuation. In the traction interruption phase (stage B), traction is cut off very quickly, so the acceleration change is negligible compared with the train's inertia, and the curve appears nearly linear. The train then enters the constant speed stage (stage C). There is no traction and braking has not been built up, so it runs briefly at a constant speed v_1 for a duration t_i . In the braking establishment stage (stage D), the braking system begins to establish pressure, and the deceleration gradually transitions from zero to the designed emergency braking level. The train then enters the braking stage (stage E) and brakes with a constant deceleration a_b until it comes to a full stop.

Also in this figure, Automatic Train Protection (ATP) monitors train speed and ensures that the train can stop safely before the Mobile Authorization Endpoint. The solid ATP curve defines the permitted speed boundary, and the dashed ATP overspeed monitoring curve is the supervision trigger threshold. It is usually set slightly above the profile to absorb measurement errors and tiny speed fluctuations, so that the small overshoots do not trigger braking. Because the

delays in the braking process are already taken into account when the ATP curves are defined, the braking curve does not fall below the ATP supervision curves, and safety can still be ensured.

By accumulating the displacements of each stage, the total braking distance from the trigger of braking to the complete stopping can be obtained:

$$d_{\text{break}} = d_A + d_B + d_C + d_D + d_E \quad (2.1)$$

Each of them can be calculated as:

$$d_A + d_B = v_0(t_r + t_m) + \frac{1}{2}a_m(t_r + t_m)^2 \quad (2.2)$$

$$d_C = v_1 t_i \quad (2.3)$$

$$d_D = v_2 t_b - \frac{1}{4}a_b t_b^2 \quad (2.4)$$

$$d_E = \frac{v_3^2}{2a_b} \quad (2.5)$$

The speed of each stage is given by the following formula:

$$v_1 = v_0 + a_m(t_r + t_m) \quad (2.6)$$

$$v_2 = v_1 \quad (2.7)$$

$$v_3 = v_2 - \frac{a_b t_b}{2} \quad (2.8)$$

This model reflects the complete braking process of the train under the most unfavorable conditions, and can be used to determine the maximum initial speed and braking distance required for safe stopping, and it is also the basis for analyzing dynamic inter-train spacing.

Reference [14] further extended the single train safety braking process to the VC scenario, and established the minimum spacing model of two trains under

emergency braking conditions. The basic idea is that in the case where two trains have different initial speeds, different braking capabilities, and communication delays, the minimum safety spacing is derived by comparing the braking distances of the two extreme cases: the most favorable braking of the leader train (direct deceleration) and the most unfavorable braking of the following train (based on the typical safety braking model above, where delays may cause the train's speed to increase briefly before decreasing).

To this end, the concepts of extra distance, maximum/minimum braking distance and safety margin are introduced. The spacing under the most unfavorable conditions is expressed as:

$$d_{\min} = l_{\text{extra}} + l_{\max}^h - l_{\min}^g + d_{\text{stop}} \quad (2.9)$$

In the formula, l_{extra} represents the distance that the following train continues to run during the period from when the leader train begins braking to when the rear train also starts braking. l_{\max}^h is the maximum braking distance of the rear train under the most unfavorable conditions. l_{\min}^g is the minimum braking distance of the front train the most favorable conditions. d_{stop} is the safety margin reserved after the two trains stop completely. Figure 2.8 intuitively shows the corresponding relationship of the distances mentioned above.

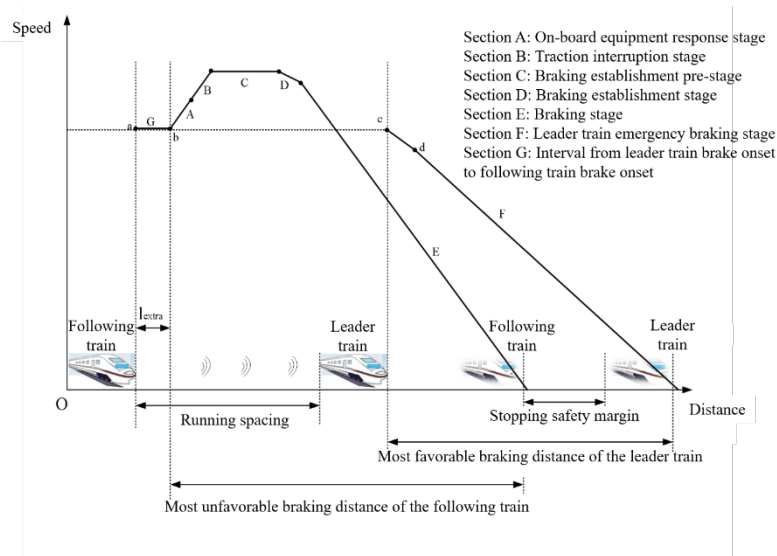


Figure 2.8 Safety braking model in virtual coupling

So if the typical safety braking mode is substituted into l_{min}^h and l_{min}^g and then simplified, the minimum spacing can be further simplified. After sorting out the given typical Communication Based Train Control (CBTC) system parameters, the empirical formulas are as follows:

$$d_{min} = \frac{1}{2a_b} \left(\frac{(v^h)^2}{3.6^2} - \frac{(v^g)^2}{3.6^2} \right) + (T_{equiv} + t_{delay}) \frac{v^h}{3.6} + C_{margin} \quad (2.10)$$

Here, a_b is the emergency braking deceleration of the following train under the most unfavorable conditions. T_{equiv} is the equivalent reaction time, which integrates the delay of driver and equipment response, control operation and braking establishment. C_{margin} is the combination of parking spacing, positioning error and other safety margins.

Once this derived formula is applied using the braking performance and communication delay conditions relevant to this study, the resulting minimum spacing can be regarded as the safety boundary and target spacing under VC operation. It should be noted that this spacing is not used to directly limit the fixed distance between the two trains along the entire route, but to provide a quantifiable reference for the subsequent driving strategy design. Therefore, when constructing the driving strategy of the following train in subsequent chapters, the control will take this spacing as the constraint condition, which means when the predicted spacing approaches the lower limit, the controller will make adjustments through traction or braking to guide the train to achieve safe and efficient following behavior.

2.4 Control architecture in virtual coupling

In real operation, maintaining a safe inter-train spacing over time also requires an appropriate control architecture and communication topology, so that the following train can respond promptly to the leader train's state with limited communication delay. Therefore, this section reviews these two aspects and, with reference to a two-train heavy haul scenario, formulates the modelling assumptions adopted in this study.

In terms of longitudinal dynamic behavior, railway trains are similar to road vehicles; consequently, many studies draw on vehicle platooning control and vehicle-to-vehicle communication technologies [15,18-20,21], and further extend the concept of VC to ultra-high-speed systems such as maglev trains and Hyperloop [15,21].

At the control level, existing work generally classifies the control architecture into two main categories: centralized and decentralized architectures [16].

Under a centralized control architecture, the entire VC train group is managed by a single central control unit, typically a Centralized Traffic Control (CTC) center. Each train periodically transmits its position, speed, acceleration and braking status to the CTC via train-to-infrastructure (T2I) communication links. The CTC then solves an optimization problem from a global information, considering safety constraints and operating efficiency, and generates the speed profiles and target spacing for all trains in the group [22]. The main advantage of this scheme is that it can explicitly account for the cooperative behavior of the entire train fleet, enabling globally optimal or near-optimal operating strategies. However, it relies heavily on communication reliability and latency, and is vulnerable to single-point failures.

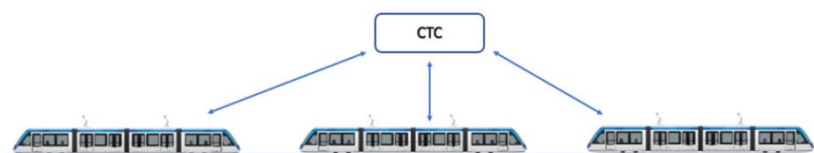


Figure 2.9 Centralized control architecture

In contrast, a decentralized control architecture assumes that each train is equipped with a local controller, and coordination through a leader–follower relationship among the trains. In one typical scheme, each train uses predicted trajectories and state information received from the train ahead to independently determine its own traction and braking commands, thereby realizing cooperative control based on local information [23]. In another scheme, the leader train plans the reference speed profile and target spacing, and then sends the following commands to the subsequent trains via train-to-

train (T2T) communication links [24]. In both schemes, the control of multi-train systems is usually modelled as a one-dimensional networked dynamical system. Compared with centralized architecture, decentralized architecture offers better structural scalability and is less prone to single-point failures, making them suitable for scenarios with a small number of trains where the trajectory of the leader train can be treated as an exogenous signal [25,26].

This study considers a two-train virtual coupling scenario. Since the number of trains is small and each train can determine its own traction and braking commands, a decentralized leader–follower architecture is more consistent with engineering practice. The leader train is not affected by the control strategy of the following train, while the following train receives the leader train’s state and adjusts its own traction and braking using the safety braking model developed in the previous section, so as to dynamically track the target inter-train spacing.

After deciding the control architecture, it is still necessary to specify how information is exchanged between trains, namely the communication topology. The communication topology defines the direction and scope of information flow among trains, affects the minimum achievable inter-train spacing, and forms a key element in the stability analysis of multi-train systems. In existing literature, the basic communication topologies most commonly adopted include unidirectional, bidirectional and non-successive communication [25,26].

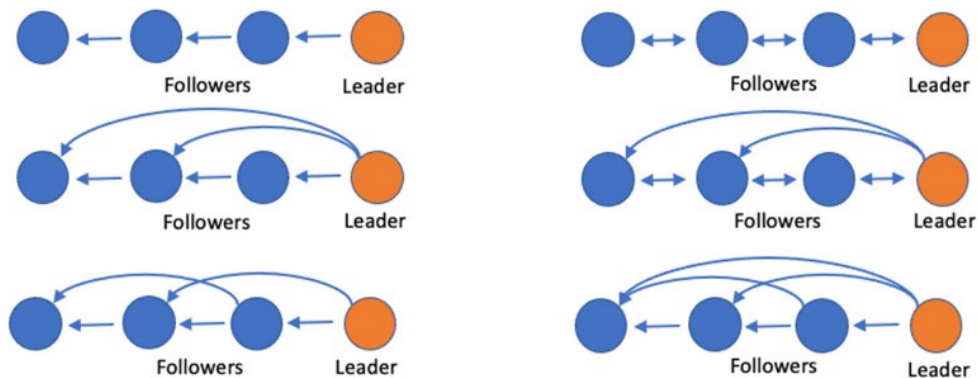


Figure 2.10 Communication topologies

Figure 2.10 illustrates typical examples, where the left side is the unidirectional topology and the right side is the bidirectional one. Considering the two-train scenario investigated in this study and the engineering context of heavy-haul railways, the discussion can be restricted to these two basic forms.

(1) Unidirectional communication topology

The key feature of this topology is that information flows only from the leader train to the following train. In a multi-train formation, the leader train broadcasts its speed, position, acceleration and other states to the following train via wireless links, while no feedback is exchanged among the following trains. In this two-train scenario, this topology reduces to one-way state transmission from the leader train to the following train, and the leader train's control is independent of the following train's operating state. This scheme is simple and places modest demands on communication bandwidth and protocol design [25,26].

(2) Bidirectional communication topology

This topology allows two-way information exchange: the leader train sends its state to the following train, and simultaneously receives feedback from the following train. For our two-train scenario, this means that the leader train considers not only its own operating strategy, line conditions and dispatch commands, but also the states of the following train during operation. The bidirectional topology can suppress string instability, meaning that small speed or spacing disturbances from the leader train are less likely to be amplified in the response of the following train, improve disturbance attenuation, and reduce fluctuations in longitudinal traction forces [25,26]. However, it imposes stricter requirements on communication delay, synchronization accuracy and control algorithm complexity, and is therefore more suitable for scenarios with complex control objectives [23, 28,29].

In conclusion, the subsequent modeling and simulations adopt a decentralized control architecture with a unidirectional communication topology as the basic assumption: the leader train does not receive feedback from the follower, while

the following train acquires the leader's speed, position and other state variables via one-way communication in real time, and designs and adjusts its own traction and braking strategy under the constraints of the safety braking model and the minimum safe spacing constraint, so as to dynamically track the target inter-train spacing and optimize train operation performance.

2.5 Control methods for virtual coupling driving strategies

To meet the need for small inter-train spacing operation under VC, the control methods can be grouped into four categories: classical feedback control, predictive control, cooperative/distributed control and intelligent control. Each category is associated with specific modelling assumptions and control objectives, and they provide a methodological basis for designing driving strategies under VC.

(1) Feedback control

In VC, feedback control is usually modelled using a standard block diagram below: the desired state is compared with the measured state to form an error signal, which is processed by a controller to generate the control input acting on the longitudinal dynamics of the train (plant), while the resulting output is fed back to close the loop.

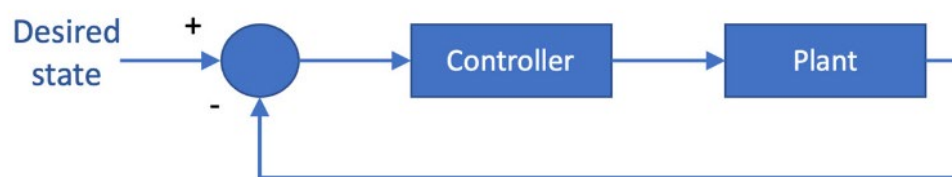


Figure 2.11 Feedback control

A typical linear feedback law can be written as

$$u(t) = K_p e(t) + K_I \int_0^t e(\tau) d\tau + K_D \frac{de(t)}{dt} \quad (2.11)$$

Here, $e(t)$ represents the speed error, the inter-train spacing error, or a weighted combination of them [32-34]. In VC, many studies adopt nonlinear mappings. For example, artificial potential fields (APF) based on hyperbolic tangent functions are used to map the speed difference and its integral into

“attractive/repulsive forces” to regulate the spacing [35,36]. In the remainder of this work, both a linear PID feedback structure and an APF-based nonlinear feedback structure are employed for comparative analysis

(2) Predictive control

Predictive control is often described as three components: model prediction, constraints, and an optimizer. The model predicts the future output trajectory based on the current state and a candidate control sequence, and the constraints impose hard or soft limits such as safety spacing and traction/braking forces. The optimizer then searches, over a finite prediction horizon, for the control sequence that minimizes a given cost function [22,28,29].

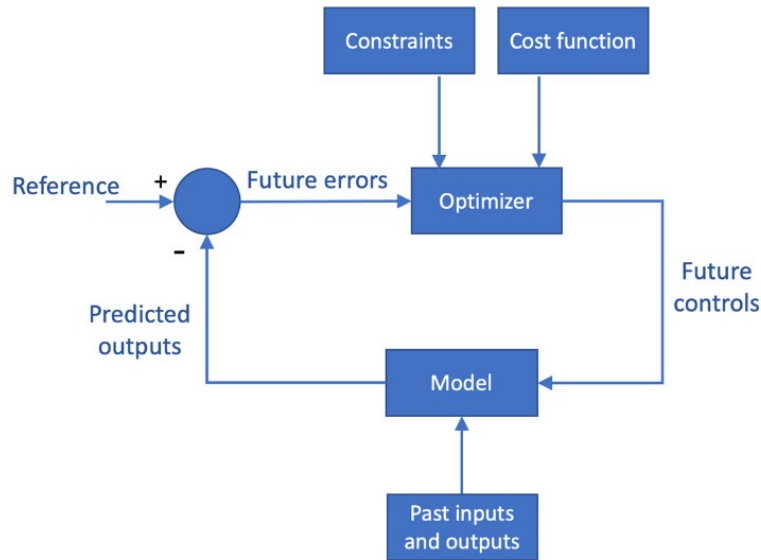


Figure 2.12 Model predictive control

A common form of the cost function can be written as:

$$\min_{u(k), \dots, u(k+N)} \sum_{i=1}^{N_p} \|y_{\text{ref}}(k+i) - y(k+i)\|^2 + \lambda \|u(k+i)\|^2 \quad (2.12)$$

In this study, we adopt a structurally similar but simplified predictive controller with a short prediction horizon. It predicts the inter-train spacing over a short future window, and incorporates both inter-train spacing safety and acceleration smoothness into the cost function, so that the predictive concept is naturally integrated with the feedback potential field.

(3) Consensus / Cooperative control

$$\dot{x}_i = f_i(x_i) + \sum_{j \in N_i} a_{ij}(x_j - x_i) \quad (2.13)$$

Here, x_i is the state of the i -th train, N_i is the set of its neighbours, and a_{ij} is the corresponding topology weights [37-39]. Such schemes can be applied to scenarios in VC such as cooperative cruising, coupling and decoupling, and arrival–departure sequencing. The two-train leader-follower system considered in this paper can be viewed as a simplified cooperative structure.

(4) Intelligent control

Intelligent control methods mainly include strategy learning frameworks based on machine learning and reinforcement learning, whose typical loop can be described as “state–action–reward–update”. In VC studies, some work employs Long Short-Term Memory (LSTM) or deep neural networks to learn complex resistance and the leader’s trajectory, and then embeds them into Model Predictive Control (MPC) or Generalized Predictive Control (GPC) for prediction. Other work adopts reinforcement learning to directly learn acceleration and deceleration strategies in a simulation, where the reward function jointly accounts for energy saving, inter-train spacing and time [40-43]. This study is still mainly based on model-driven feedback–predictive control and does not adopt such intelligent methods, but these approaches offer promising directions for future work on learning-based parameter tuning and multi-train strategy optimization.

2.6 Summary

This chapter reviews the main research lines on virtual coupling. It first traces the development from the original VC concept and the evolution of block systems, and it highlights that VC relies on high-accuracy positioning and reliable communication to support small inter-train spacing and higher line capacity. It then introduces the key components of dynamic inter-train spacing and shows that the minimum safe spacing is jointly affected by the braking capabilities of the leader and following trains, communication delay, and the

staged response process. Next, the chapter summarizes centralized and decentralized control architectures and their communication topologies, and it clarifies the main trade-offs in achievable spacing, reliability, and engineering applicability. Finally, it categorizes the commonly used control methods for VC, outlines their key features, and identifies the methods needed for the subsequent study. Overall, this chapter provides the basis for the control design and modeling developed in the following chapters.

3 Methodology

3.1 Overview of Research Framework

The study focuses on driving strategies for heavy-haul trains under virtual coupling. As shown in Figure 3.1, the overall framework consists of four stages. First, a single-train longitudinal dynamics model is developed from line information. Second, key constraints such as safety margin and some delays are introduced to extend the model to multi-train operation. Then the related driving strategies are designed based on this model. Finally, the proposed strategy is validated using data from a real railway line.

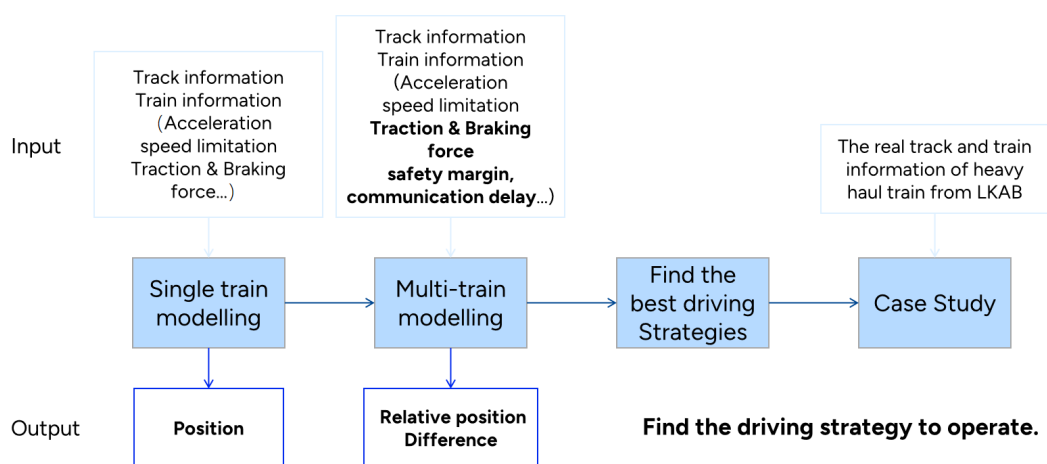


Figure 3.1 Overall methodological framework

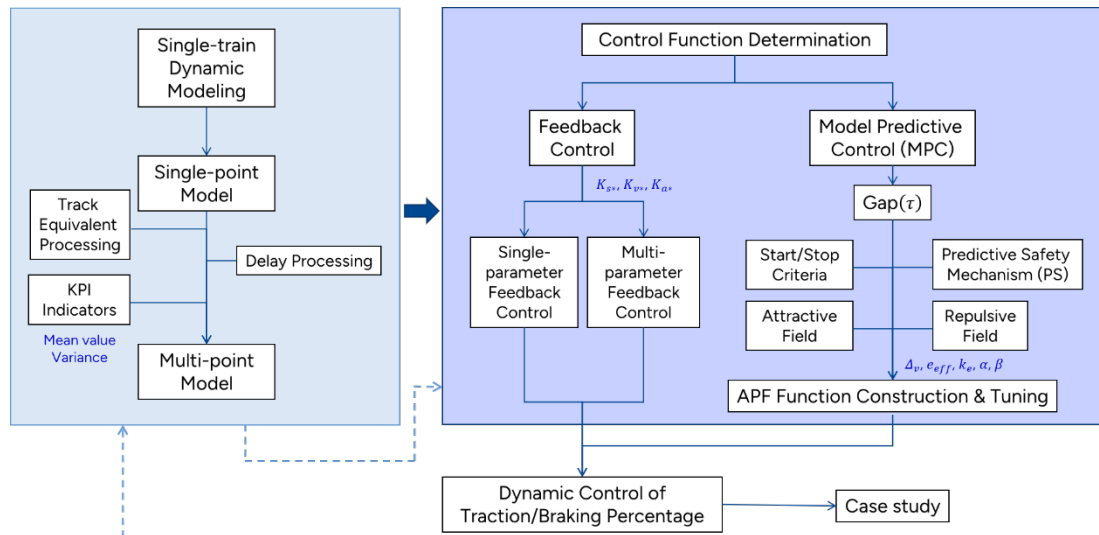


Figure 3.2 Technical roadmap for modeling and control design

Figure 3.2 further develops a technical roadmap for modeling and control design. In the left light-blue block of Figure 3.2, the study begins with single-train longitudinal dynamics modeling. The model inputs are divided into two groups: line information, including gradients, curve radius, and speed-limit profiles; and train information, including mass, maximum traction/braking force, allowable acceleration, and the operating profile. Based on these inputs, a set of longitudinal dynamics equations is established to describe how traction, braking, and running resistance jointly govern the change of train speed, position, and acceleration over time. At this stage, a traditional single-point model is used, which represents only the longitudinal motion of the train's center of mass.

The single-point model is enough for trajectory generation and macroscopic operation analysis, but it remains too idealized for small-spacing following under VC. Specifically, on the one hand, it does not consider the train-length effect, which is at a given instant, different parts of a long train may occupy different line sections, so the gradient and curvature inputs are not uniform along the train. On the other hand, it cannot reflect delays in inter-train information transmission or control execution. Therefore, the single-point model should be extended to a multi-point model. In this model, the original gradient and curve radius are converted into equivalent inputs by using a sliding window matched to the train length. In this way, the effect of spanning several line sections at the same time is represented by an equivalent gradient

and an equivalent curve radius, which are then used as external inputs to the dynamic equations, so that the length effect of heavy-haul trains can be captured.

On this basis, the single-train multi-point model is further extended to a multi-train multi-point model, with additional modules for safety margin, delay handling, and key performance indicators (KPIs), as shown on the left side of Figure 3.2. Here, multi-train means a model with several trains, which explicitly accounts for the interaction between trains, including relative motion, information exchange, and operational constraints within the train group. It should be noted that conventional communication delay, together with delays introduced by traction/braking actuation and signal feedback, is treated here as a unified “delay” term. And for the key performance indicators, the mean value and standard deviation of the inter-train spacing are used as the main measures. They describe the stability and fluctuation of spacing during train-following, and they also provide a quantitative basis for comparing different driving strategies and assessing their reliability.

The outputs of the modeling stage in the left light-blue block include not only the absolute position and speed profiles of each train, but also the relative spacing between the two trains. The process then moves to the right dark-blue block “Control Function Determination”. In this block, two control methods are developed and compared: a difference-based linear feedback control, and a nonlinear control that combines prediction with an artificial potential field (APF).

The first linear feedback control is built from differences. Both single-parameter and three-parameter feedback structures are considered. The single-parameter form uses only one variable, such as speed difference, acceleration difference, or spacing difference, while the three-parameter form combines all three to regulate the inter-train spacing.

The second one is nonlinear predictive control. Here, a short-horizon predictive layer is first introduced as an initial spacing-regulation step. It predicts the future instantaneous inter-train spacing over a short time window τ , denoted by $gap(\tau)$, based on the current states of the leader and following trains. This predicted spacing is then used to determine the maximum allowable safe acceleration. When the predicted spacing is likely to approach or fall below the safety threshold, the corresponding mechanism is activated to gradually reduce traction and strengthen braking. Then an APF function is introduced to generate the final acceleration command. It regulates spacing through an attractive field and a repulsive field. When the spacing is too large, the attractive effect encourages the following train to close the gap. When the spacing approaches the lower safety bound, the repulsive effect becomes stronger and suppresses further acceleration.

The controller output is finally mapped into percentage allocation across three channels, namely traction, regenerative braking, and mechanical braking. Here, percentage allocation means that the control command is expressed as the relative share assigned to each channel, rather than as an absolute force value. In this way, the controller determines how much of the required longitudinal action should be provided by traction, regenerative braking, and mechanical braking, thereby forming a dynamic force distribution model.

Finally, the above modeling and control modules are applied to real operating data from the Swedish LKAB heavy-haul line. Simulations are carried out using real line parameters and IORE heavy-haul train data, and different driving strategies are compared in terms of safety margin, spacing fluctuation, and related indicators to assess the applicability of the proposed control strategies in engineering practice.

3.2 Simulation Tool

The whole study uses numerical simulation as the primary analysis tool. On the one hand, it enables full use of the available real track data and train data; on the other hand, it allows key parameters such as safety spacing, communication

delay and driving strategy to be systematically varied, so that operating scenarios which cannot yet be tested extensively in real service can be investigated.

This work is built on the simulation tool STEC (Simulation of Train Energy Consumption), originally developed jointly by KTH Royal Institute of Technology and MiW Rail Technology AB [37]. The tool is adapted and extended, and a new simulation platform is set up by using Excel and MATLAB. On the Excel side, several worksheets are organized by function to enter and pre-process the various input data required for simulation, and to represent time-domain delay effects in an explicit form. MATLAB acts as the simulation engine, importing the Excel files, performing time-domain integration, and outputting the traction/braking percentage allocation together with the key performance indicators. This setup gives the model good readability and maintainability, while making it straightforward to change track conditions, adjust the VC driving strategy, or incorporate additional control schemes.

3.3 Data Collection

The train and track models developed in this study, as well as the subsequent model validation, rely on multiple sources of measured data and technical documentation. Overall, these inputs can be grouped into three categories: vehicle technical documents, train operation data and track data.

The train technical parameters required for model development are mainly taken from technical specifications and design manuals, including total train mass, axle load, traction performance and braking equipment. For parameters that are not explicitly given in these documentations, such as the running resistance curve, the numerical values used for modelling and simulations are taken from the results reported in Reference [39]. Besides, the train operating data mainly comes from several recording systems maintained by the operator and installed on the locomotives. The operational database provides information such as train ID, locomotive type, consist configuration and depot entry/exit times, which are used to identify typical heavy-haul trains and

representative operating conditions. The event recorders and selected high-sampling-rate test data offer higher time resolution signals, including speed, traction/braking effort and brake pressure, which are used to calibrate and validate the details of the longitudinal dynamic model and the traction and braking control behavior.

The track data required for the simulations are obtained from the infrastructure manager's database. For the sections located in Sweden, line data such as gradient and curve radius are extracted directly from Trafikverket's BIS database. These data have a spatial resolution on the order of metres and are continuously updated as the line is upgraded, so they can be regarded as a reliable representation of the current track. For the Norwegian sections, the longitudinal profile given in the locomotive tender technical specification is used. Although this document predates some recent upgrades, its deviation from the present track alignment is limited to a few newly added tunnels. In the simulations, the trains are assumed to operate on the original alignment, and the effect of these local differences on the overall behavior is negligible.

Overall, the data used in this study come from real operating lines and actual train equipment, which provides a solid basis for the subsequent dynamic simulations.

3.4 Key performance indicators (KPIs)

This study focuses the evaluation on the relative position relationship between the two trains. To avoid introducing too many indicators that may distract from the main objective, three simple but targeted key performance indicators are selected around the core variable of inter-train spacing: the instantaneous spacing between trains, the mean value of spacing, and the standard deviation of spacing.

More specifically, the spacing curve formed by the instantaneous spacing values between trains shows how close or far apart the two trains throughout the whole operation process, and it is the most direct indication of safety and

coordination. The mean value of spacing describes the general spacing level maintained over a period, and it is used to judge whether a strategy is overall conservative, with overly large spacing, or aggressive, with spacing too close to the lower safety bound. The standard deviation of spacing measures how much the spacing fluctuates around its mean level. In other words, it reflects how strongly the spacing oscillates and whether it remains stable.

When comparing different driving strategies, the primary requirement is that instantaneous inter-train spacing $d(t)$ should never fall below the prescribed safety spacing. Under this safety constraint, both the mean value and the standard deviation of the inter-train spacing are evaluated. A control strategy with a mean spacing closer to the target value and a smaller standard deviation indicates that the inter-train spacing remains closer to the desired level and that the train-following process is more stable over time.

4 Modelling

Under the given tracking inter-train spacing and control objectives, train motion under complex line conditions depends not only on control inputs such as traction and braking, but also on the combined effects of line conditions, delays, and the information-exchange pattern between trains. Therefore, this chapter systematically presents the modeling framework and implementation steps for the VC scenario, covering equivalent treatment of track geometry, train longitudinal dynamics, time-domain discretization, and the cooperative control structure of a two-train leader-follower system. These provide the basis for the subsequent analysis and simulation.

Since heavy-haul trains usually have a long train body, a single-point model, which treats the whole train as a single mass point, cannot accurately capture the force characteristics of the train on long gradients and continuous curved sections. To address this, Section 4.1 extends the classical single-point model and introduces the concept of a multi-point model to account for the effects along the train length. Based on this, Section 4.2 further formulates the longitudinal dynamics equations and the corresponding force model. Section 4.3 then proposes a time-domain treatment method for the problem that the two trains occupy different positions on the track at the same instant. Section 4.4 incorporates communication and execution delays into the modeling to describe the lag effects of information transmission and traction/braking response. On this basis, Section 4.5 builds a cooperative control model for the

two trains, which brings the above dynamics characteristics, line effects, and delay factors into one framework. Finally, Section 4.6 describes the line data, train parameters, and simulation conditions used in the case study.

4.1 Multi-point train modelling

In longitudinal train dynamics modeling, two simplified methods are commonly used: the single-point model, in which the entire train is represented as a single concentrated mass, and the multi-particle model, in which the train is discretized into multiple vehicle bodies or nodes. To balance model accuracy and computational efficiency, this study adopts a single-point dynamics framework, while introducing a multi-point model for track geometry inputs. Based on the line conditions along the train length, an equivalent curve radius and equivalent gradient are constructed.

The multi-point train model used here is distinct from the traditional multi-particle model. It does not introduce additional dynamic degrees of freedom, but only accounts for the train-length effect in the external line inputs. The following sections describe the determination of the equivalent curve radius and equivalent gradient.

4.1.1 Equivalent curve radius processing

Horizontal alignment data are usually provided in segmented form, with each segment defined by its starting mileage, segment type (straight line, circular curve or transition curve) and design radius. For subsequent simulation, the track is first divided by the given breakpoints into consecutive intervals $[s_j, s_{j+1})$, where s_j and s_{j+1} denote the starting and ending mileage of the j -th section, respectively. Here, breakpoints refer to the original mileage boundaries between adjacent alignment sections, such as the transition locations between straight lines and circular curves, and they are used to divide the track into several original sections. They are different from the uniformly spaced evaluation points generated later based on the fixed step length. Then, a representative mean curvature κ_j is assigned to each section. For a straight line, $\kappa_j = 0$. For a circular curve, $\kappa_j = 1/R_j$ based on the design radius R_j . For a transition curve, the representative curvature is approximated as the average

of the endpoint curvatures, based on the starting and ending radii $R_{j,1}$ and $R_{j,2}$, as follows:

$$\kappa_j = \frac{1}{2} (R_{j,1}^{-1} + R_{j,2}^{-1}) \quad (4.1)$$

In the multi-point train model, the train is represented by a sliding window of length L_{train} . When the train head is located at mileage s , the train occupies the interval $[s - L_{\text{train}}, s]$. Because of the train-length effect, the train may simultaneously cover multiple segments with different curvatures. For example, the train head may already have entered a circular curve, while the train tail is still on a straight line or a transition curve. Therefore, using only the curvature at a single position cannot adequately reflect the horizontal alignment experienced by the whole train. To address this, the curvatures of all sections covered by the sliding window are combined through a length-weighted average to obtain the equivalent curvature:

$$\kappa_{eq}(s) = \frac{\sum_j \kappa_j \Delta L_j(s)}{\sum_j \Delta L_j(s)} \quad (4.2)$$

Here, $\Delta L_j(s)$ is the overlap length between the window $[s - L_{\text{train}}, s]$ and the j -th track segment $[s_j, s_{j+1})$. In numerical implementation, evaluation points s_k are generated along the track at a fixed step length, and the above equation is applied at each s_k to obtain the equivalent curvature sequence $\kappa_{eq}(s_k)$. The equivalent curve radius is then determined from $\kappa_{eq}(s)$. When $\kappa_{eq}(s)$ is zero or close to zero, the track can be regarded as approximately straight, and the equivalent radius is taken as infinity. Otherwise, the equivalent radius is defined as the reciprocal of the equivalent curvature:

$$R_{eq}(s) = \begin{cases} +\infty, & \kappa_{eq}(s) = 0, \\ \left| \frac{1}{\kappa_{eq}(s)} \right|, & \kappa_{eq}(s) \neq 0. \end{cases} \quad (4.3)$$

Through this treatment, the stepwise variation in the original curve radius input is converted into a smooth equivalent radius curve that varies continuously along the track. This allows the horizontal alignment input to better reflect the overall geometric conditions encountered by a long train spanning several curve sections, while the underlying longitudinal dynamics remain within a single-point modeling framework.

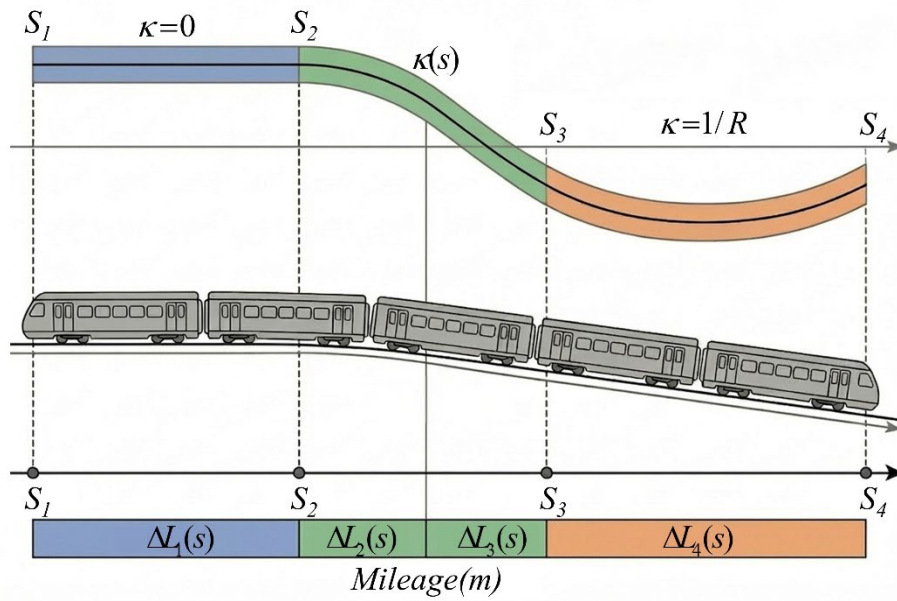


Figure 4.1 Schematic illustration of equivalent curve radius calculation in the multi-point train model

4.1.2 Equivalent gradient processing

Vertical profile data are usually provided in the form of mileage–elevation pairs. For a long heavy-haul train, using only the instantaneous gradient at the current reference position to calculate traction resistance and braking demand ignores the fact that the head and tail may lie on different gradient sections. For instance, when the train head has just passed the highest point of the ramp while the tail is still on the upgrade, the effective gradient acting on the whole train differs substantially from the local gradient at the head.

To account for this, the equivalent gradient is constructed using the same sliding-window idea. When the train head is located at mileage s , the train occupies the interval $[s - L_{\text{train}}, s]$. In the continuous case, the equivalent gradient is defined as the elevation difference across the window divided by the train length:

$$G_{eq}(s) = \frac{H(s) - H(s - L_{\text{train}})}{L_{\text{train}}} \times 1000 \quad (4.4)$$

Here, $H(s)$ is the elevation of the track vertical profile at mileage s , and $G_{eq}(s)$ is the equivalent gradient, expressed in per mille (‰). A positive value indicates an upgrade, whereas a negative value indicates a downgrade. Its absolute value represents the mean longitudinal gradient experienced by the whole train.

In practice, the original discrete mileage-elevation points of the vertical profile are often unevenly spaced and may contain small local fluctuations. To improve numerical stability, the elevation data are first interpolated at a fixed step length to obtain a smoothed sequence $\tilde{H}(s)$. The same head–tail elevation-difference definition is then applied to the interpolated profile:

$$G_{eq}(s) = \frac{\tilde{H}(s) - \tilde{H}(s - L_{train})}{L_{train}} \times 1000 \quad (4.5)$$

where $\tilde{H}(s)$ is obtained by linear interpolation. For numerical implementation, the calculation may be adjusted according to the relation between the interpolation step length and the train length. When the step length is smaller than the train length, the elevation differences of several adjacent interpolated points within the window can be accumulated and divided by the total length to obtain the mean gradient. When the step length is comparable to the train length, the elevation difference between the train tail and head can be used directly.

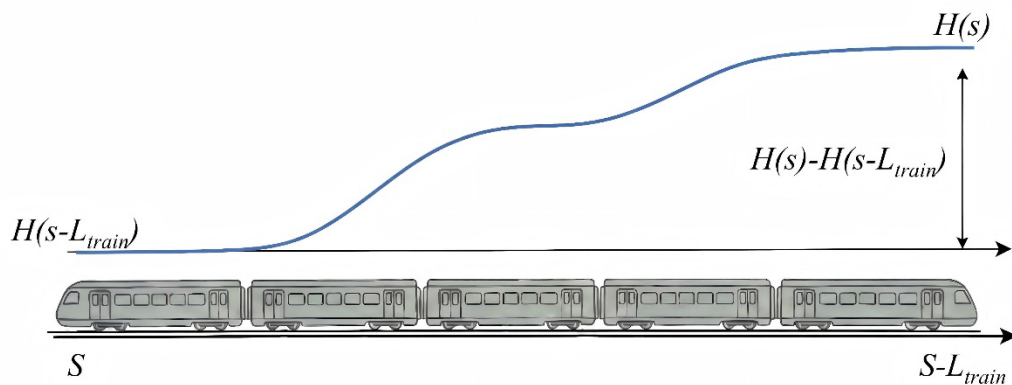


Figure 4.2 Schematic illustration of equivalent gradient calculation in the multi-point train model

Through this treatment, a smoother equivalent gradient profile $G_{eq}(s)$ is obtained, so that the vertical profile input can better capture the train-length effect over multiple gradient segments.

4.2 Dynamic modelling

4.2.1 Model assumption

To simplify the problem while maintaining physical plausibility and improving simulation efficiency, the following assumptions are introduced for the train system and track conditions before establishing the model:

- (1) The train is assumed to move only along the track direction; lateral and vertical degrees of freedom are neglected. The entire train is abstracted as a rigid body, without explicitly modeling coupler elasticity or the coupling between aerodynamics and vehicle attitude.
- (2) Environmental parameters are taken as constant.
- (3) Track parameters are processed using the sliding-window method described earlier.

4.2.2 Dynamic model assumption

Based on the above choice of a point-mass model, the longitudinal force diagram of the train is shown in Figure 4.3.

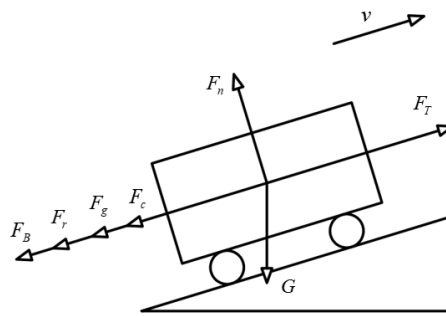


Figure 4.3 Force analysis of the train during operation

The longitudinal dynamics of the train can be written as:

$$ma = F_T - F_B - F_r - F_g - F_c \quad (4.6)$$

Here, F_T is the traction force provided by the locomotive, F_B is the braking force generated by the braking system, F_r is the running resistance, F_g is the gradient resistance, F_c is the curve resistance, F_n is the normal force exerted by the track on the train, and G is the gravitational force acting on the train.

4.2.3 Traction force calculation

Traction force is the primary driving force that enables the train to overcome resistance and sustain motion. Its magnitude depends on the locomotive drive system, wheel–rail adhesion and transmission efficiency. In this study, the locomotive is an IORE AC electric locomotive, whose rated traction force is approximately 1200 kN. During start-up, the maximum traction force can reach 1400 kN; however, this level is mainly used under special operating conditions, such as low-speed operation on steep gradients, and is therefore excluded from the present simulations. The traction characteristic is shown in Figure 4.3, and the fitted relationship between speed v and traction force F_T is given by:

$$F_T(v) = \begin{cases} 1200 & 0 \leq v \leq 32 \\ -16694.5407v^{0.03994} + 20335.7893 & 32 < v \leq 79 \\ -22.9091v + 2052.727 & 79 < v \leq 90 \\ 0 & v > 90 \end{cases} \quad (4.7)$$

Here, $F_T(kN)$ is the train traction force; $v(km/h)$ is the locomotive running speed.

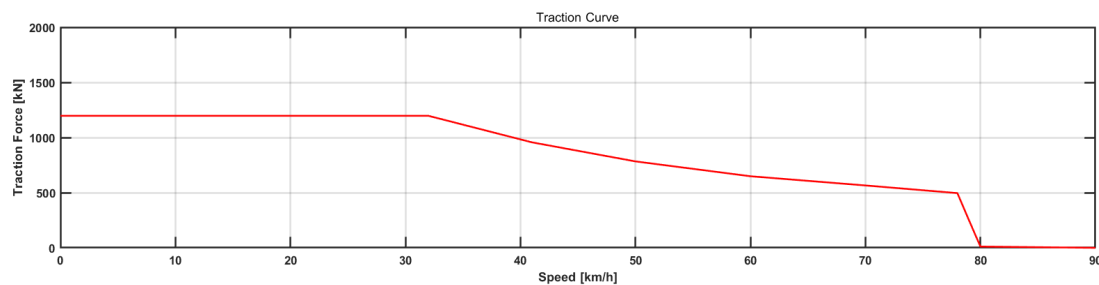


Figure 4.3 Traction characteristic curve

4.2.4 Braking force calculation

The train braking force is jointly supplied by regenerative braking and mechanical braking. Regenerative braking recovers part of the kinetic energy through the traction motors operating in generating mode and is generally more effective at higher speeds or under lighter loads. Mechanical braking is generated by friction braking devices and plays a dominant role at low speed

and during final stopping. In typical operation, regenerative braking contributes more at high speed, whereas mechanical braking becomes increasingly important at low speed, under heavy-haul conditions, or when the regenerative braking capacity is limited. The braking characteristic used in this study is shown in Figure 4.4.

$$F_B = F_{Bregen} + F_{Bmech} \quad (4.8)$$

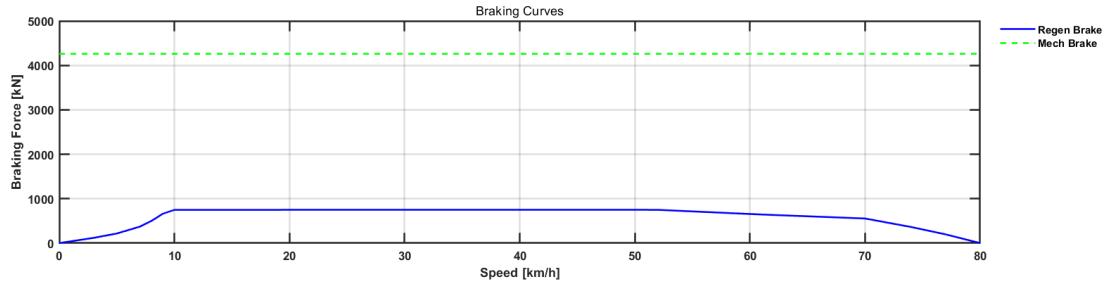


Figure 4.4 Braking characteristic curve

4.2.5 Running resistance calculation

During operation, a train is subjected not only to traction and braking forces but also to various external resistances, collectively referred to as running resistance. The main components of running resistance include rolling resistance, bearing friction, losses in the motors and transmission system, and aerodynamic drag. All these forces act opposite to the direction of motion and exhibit different growth patterns with increasing speed. The Davis model is adopted to represent them in a unified form within the longitudinal dynamic model. Accordingly, the running resistance is expressed as a polynomial function of speed:

$$F_r = C_0 + C_1v + C_2v^2 \quad (4.9)$$

For the IORE heavy-haul train considered in this study, the running resistance coefficients are taken from the literature, where they were determined using the Transrail formula together with the train data [44]: $C_0 = 51106$, $C_1 = 149.6$ and $C_2 = 102.62$. Here, C_0 is the speed-independent constant term, mainly accounting for rolling resistance, mechanical friction and the basic consumption of fans and auxiliary equipment. C_1 is the coefficient of the term proportional to speed, representing additional losses that increase moderately with speed, such as magnetic losses in the motors and changes in lubrication

conditions. C_2 is the aerodynamic resistance coefficient, which becomes increasingly important at higher speeds and causes the resistance to grow with the square of speed.

It can be seen that C_0 dominates at low speed, while the influence of the linear term C_1v becomes more pronounced in the medium speed range. At higher speeds, aerodynamic resistance becomes dominant, making the quadratic term C_2v^2 the decisive component.

4.2.6 Gradient resistance calculation

Gradient resistance is the longitudinal force caused by the component of gravity along the track when a train runs on a grade. When the train climbs, this component acts opposite to the direction of motion and increases the resistance to be overcome. When the train descends, it acts in the direction of motion and therefore reduces the required traction effort.

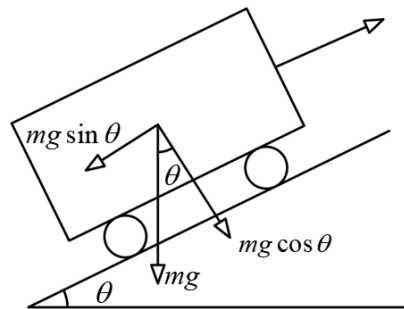


Figure 4.5 Schematic diagram of gradient force decomposition

As shown in Figure 4.5, when a train with mass m runs on a track with gradient angle θ , its weight mg can be decomposed into a component $mg \cos \theta$ normal to the track and a component $mg \sin \theta$ along the track. The latter corresponds to the gradient resistance F_g . Railway gradient is usually expressed in per mille (‰). For railway lines with small gradient, the approximation $\sin \theta \approx \tan \theta$ can be applied, so that:

$$\tan \theta \approx \frac{\text{Gradient}}{1000} \quad (4.10)$$

Substituting this relation into the above expression gives the gradient resistance acting on the train along the track:

$$F_g = mg \sin \theta \approx mg \frac{\text{Gradient}}{1000} \quad (4.11)$$

4.2.7 Curve resistance calculation

When a train passes through a curved track section, the geometric mismatch between wheel and rail, together with the associated lateral interaction forces, gives rise to additional wheel-rail friction and other curve-related losses. These effects produce an additional longitudinal resistance, referred to as curve resistance. Curve resistance is governed mainly by the curve radius: the smaller the radius, the stronger the wheel–rail interaction and the larger the additional resistance. By contrast, when the curve radius is sufficiently large, the track can be regarded as approximately a straight line, and the curve resistance can be neglected.

A commonly used expression for curve resistance is given by:

$$F_c = \begin{cases} \frac{6.5}{R-55} & R < 300\text{m} \\ 0 & R \geq 300\text{m} \end{cases} \quad (4.12)$$

where R is the curve radius (m) and m is the train mass (kg).

4.3 Time-domain treatment

In the VC simulation, both trains use a unified time step Δt to advance synchronously on the same time grid, so that the system state is updated synchronously at the instants $t_n = n\Delta t$. Let $s_i(t_n)$ denote the longitudinal position of train i at time t_n ($i = 1, 2$). Although the two trains share the same simulation time, they generally occupy different locations on the track because of their different initial positions and operating states. To describe the relative spatial relationship between the two trains, let $\Delta s_{\text{ref}}(t_n)$ denote the prescribed inter-train spacing used for track-input. Then the spatial position of train 2 can be written as

$$s_2(t_n) \approx s_1(t_n) - \Delta s_{\text{ref}}(t_n) \quad (4.13)$$

This means that, at the same time instant, the two trains should read track inputs from different locations on the same track. For any track input quantity $Q(s)$, such as the equivalent curve radius $R_{eq}(s)$, equivalent gradient $G_{eq}(s)$, or speed limit $V_{lim}(s)$, the corresponding input for train i is defined by

$$Q_i(t_n) = Q(s_i(t_n)), \quad i = 1, 2 \quad (4.14)$$

and thus, for train 2:

$$Q_2(t_n) = Q(s_1(t_n) - \Delta s_{ref}(t_n)) \quad (4.15)$$

This relation can be interpreted as time-synchronized but space-shifted track inputs, which is the two trains run on the same time axis, while each train reads track information at its own spatial position. The concept is illustrated schematically in Figure 4.6.

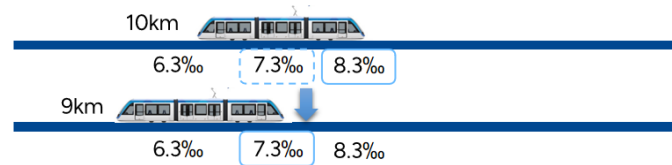


Figure 4.6 Schematic illustration of time-synchronized but space-shifted track inputs

To enable $Q(s)$, the track is discretized by breakpoints into intervals $[s_k^b, s_{k+1}^b)$, where s_k^b denotes the k -th breakpoint. Each interval is assigned to the corresponding values of equivalent curve radius, equivalent gradient, speed limit, and other track related inputs. At each time step, the input for each train is obtained from the interval containing its current position. In this way, both trains use the same underlying track description, but sample it at different spatial locations determined by their relative positions, as shown in Figure 4.7.

Train 1					Train 2				
Breakpoint	Curve Radius(m)	Gradient (‰)	Other inputs	Breakpoint	Curve Radius(m)	Gradient (‰)	Other inputs
s_k^b	6526	-8.30			s_k^b	5624	-6.98		
s_{k+1}^b	1977	-9.96	↓ Input shift due to Δs_{ref}		s_{k+1}^b	6526	-8.30		
s_{k+2}^b	2693	-5.37		s_{k+2}^b	1977	-9.96			
s_{k+3}^b	4478	-6.41			s_{k+3}^b	2693	-5.37		
.....		
s_{k+n}^b	$R_{eq}(s)$	$G_{eq}(s)$			s_{k+n}^b	$R_{eq}(s)$	$G_{eq}(s)$		

Same time step, different spatial sampling positions

Figure 4.7 Schematic illustration of position dependent track input

It should be noted that the control laws developed in this study are formulated in the time domain using variables such as speed and acceleration, rather than absolute distance as a direct control input. Therefore, the present time-domain treatment does not alter the control law itself. It only ensures that the track-related inputs remain consistent with the actual spatial positions of the two trains. This provides a unified time-space representation for the subsequent simulation.

4.4 Communication and actuation delay processing

In VC operation, time delays arise inevitably from communication, on-board processing, and actuator response. If all these delays were neglected, traction and braking commands would be assumed to take effect instantaneously, which would be overly idealized, but modelling every individual delay separately would make the framework unnecessarily complicated. Therefore, the dominant delay mechanisms are aggregated into a small number of equivalent delay quantities.

Representative time constants used in this aggregation are listed in Table 4.1. From a physical perspective, they can be grouped into two categories. The first is communication and control delay, including the on-board equipment response time $t_{response}$ and the train communication delay t_{delay} , both typically on the order of 0.1–0.2 s. The second is actuation delay, including the traction or braking release time $t_{release}$, the emergency brake dead time $t_{inertia}$, and the brake build-up time t_{build} , which are usually around 1 s. It is worth

noting that the meaning of $t_{inertia}$ is the dead time before the emergency brake begins to generate effective braking force, and t_{build} is the time required for the braking force to build up to its effective level.

Since the study focuses on train motion over time scales of tens to hundreds of seconds, the short time 0.1 s is not modelled separately, but absorbed into equivalent delays. Accordingly, two aggregate delay parameters are introduced, namely the traction delay T_{trac} and the braking delay T_{brake} , which are taken as approximately 1 s and 2 s, respectively, in the baseline simulation and are further treated as tunable parameters in the analysis.

Table 4.1 Representative time constants used in delay modelling

Parameter	Symbol (Unit)	Value
On-board equipment response time	$t_{response}(s)$	0.2
Traction (or braking) release time	$t_{release}(s)$	0.1
Emergency brake dead time	$t_{inertia}(s)$	1
Braking build-up time	$t_{build}(s)$	1
Train communication delay time	$t_{delay}(s)$	0.1

To incorporate delay into the breakpoint-based track-input framework established in Section 4.3, the time delay is converted into an equivalent spatial lag. Here, we assume that Δs_{bp} is the spacing between two adjacent breakpoints, and $v(t)$ is the current train speed. Under a delay T , the train travels an additional distance

$$\Delta s_{delay} = v(t)T \quad (4.16)$$

The spatial lag can be converted to breakpoint row offset, that is

$$N_{\text{offset}}(v, T) = \frac{\Delta s_{\text{delay}}}{\Delta s_{\text{bp}}} = \frac{v(t)T}{\Delta s_{\text{bp}}} \quad (4.17)$$

Equation 4.17 gives a continuous relation between train speed and the row offset. However, in the discrete implementation, breakpoint rows can only be indexed by non-negative integers. Therefore, the continuous value of $N_{\text{offset}}(v, T)$ must be quantized to an integer before it is applied to the calculation. As a result, the speed–offset relation becomes piecewise constant rather than continuous, which gives rise to the staircase curves shown in Figure 4.8.

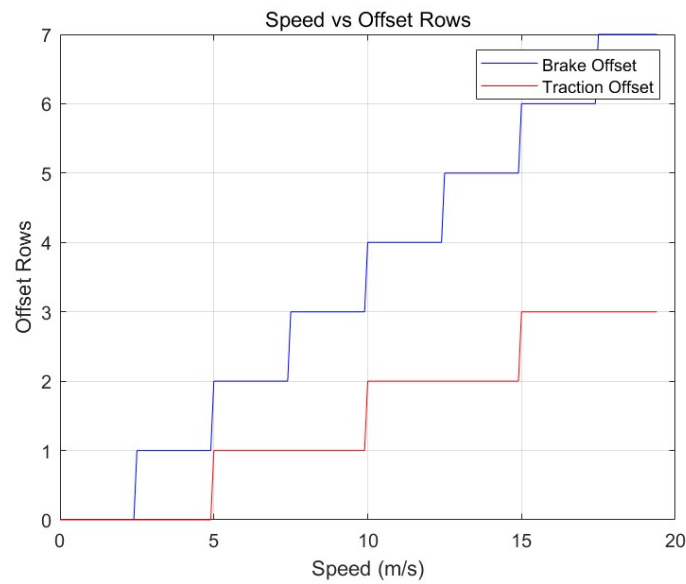


Figure 4.8 Speed–offset rows curves

This staircase representation is a consequence of breakpoint discretization and integer row indexing. It also brings some advantages in the simulation. Since the train speed is usually steady over the whole journey, small speed fluctuations do not necessarily require the offset row number to change at every instant. Using a piecewise row offset avoids frequent switching of the track input, reduces unnecessary computational effort, and improves numerical robustness.

Because the equivalent traction and braking delays are different, two separate speed–offset mappings are defined, namely $N_{\text{trac}}(v)$ and $N_{\text{brake}}(v)$. During simulation, the current speed is used to determine the corresponding offset row

number, which is then combined with the spatial shift introduced in Section 4.3. In this way, communication delay, actuation delay, and inter-train spacing are represented within a unified breakpoint-based framework.

4.5 Two-train cooperative control model

Building on the modelling framework established above, a two-train cooperative control model is further developed. In this thesis, the term “driving strategy” refers specifically to the integrated cooperative control framework for the following train within this model. It consists of five modules: track-dependent preprocessing rules, finite-horizon inter-train spacing prediction, predictive safety control, velocity-based APF control, and stop–restart control. The following subsections introduce these modules in sequence.

4.5.1 Preprocessing rules

Before introducing the cooperative control of two trains, the longitudinal forces are first preprocessed according to the track conditions. For a given locomotive, the three longitudinal force generation channels, namely traction, regenerative braking, and mechanical braking, each have their own speed-dependent force characteristics, denoted by $F_{i,\max}(v)$ ($i \in \{T, R, M\}$). These curves are determined by the locomotive and braking characteristics and describe the maximum output available from each channel at a given speed.

However, in actual operation, the train does not always work at the maximum traction or braking force allowed by the current speed. Instead, the force level must be adjusted according to track-related factors such as gradient, curve radius, speed limit, and safety margin. To incorporate these track effects in advance, and thereby reduce the computational burden of the subsequent control, the position-dependent percentage factors $\eta_i(s) \in [0,1]$ are defined, and the preallocated force of each channel is constructed as

$$F_{i,pre}(s) = \eta_i(s)F_{i,\max}(v(s)), \quad i \in \{T, R, M\} \quad (4.18)$$

where $\eta_i(s)$ denotes the preprocessing percentage factor of channel i at position s . Here, the term “channel” refers to a longitudinal force generation channel, namely traction, regenerative braking, or mechanical braking. The

equation above means that the speed-dependent maximum capability of each channel is first determined from the traction and braking characteristic curves, and is then scaled by the preprocessing factor $\eta_i(s)$ to obtain the preallocated force at that location.

It should be noted that the preallocated force defined here represents a baseline force level generated in advance from the track conditions, rather than the final output of the subsequent cooperative control. In other words, the later control does not solve the traction or braking force entirely from scratch, but performs further correction and fine adjustment on the basis of these preallocated forces. In this way, the part strongly related to the track environment and varying relatively slowly is processed in the preprocessing stage, so that the follow-up control can focus more on the fast dynamic coordination between the two trains.

The preprocessing rules are established in two steps. First, based on the equivalent gradient $G_{eq}(s)$ obtained in Section 4.1.2, the line is divided into several gradient ranges, and baseline preallocation ratios are assigned to $\eta_T(s)$, $\eta_R(s)$, and $\eta_M(s)$, as listed in Table 4.2. These ratios are not the actual output forces. Instead, they provide initial channel preferences for the subsequent simulations. Then, the baseline values are further corrected according to the equivalent curve radius $R_{eq}(s)$ obtained in Section 4.1.1, as listed in Table 4.3.

Table 4.2 Gradient-dependent preprocessing rules for force channels

Gradient (%)	Traction ratio (%)	Mech Brake ratio (%)	Regen Brake ratio (%)	Description
≤ -6	0	70	100	Long downhill; strong forced deceleration, prioritize regeneration + mechanical supplement
$-6 < \text{Gradient} \leq -3$	25	50	100	Moderate downhill; mainly regen braking, with mech compensation
$-3 < \text{Gradient} < 0$	50	30	100	Slight downhill; requires certain braking balance
$= 0$	100	0	0	Horizontal section; full traction
$0 < \text{Gradient} < 3$	100	0	0	Slight uphill
$3 \leq \text{Gradient} < 6$	100	0	0	Moderate uphill; increases traction
≥ 6	100	0	0	Steep uphill; strong traction to prevent excessive deceleration

Table 4.3 Curve-dependent preprocessing rules for force channels

Curve Radius (m)	Revision Note	Revision Strategy (Correction Factor)
< 1000	Excessively sharp curve, high resistance	If Traction > 0 : increase by 10%; If Brake > 0 : increase by 10%
1000–3000	Moderate curve	If Traction > 0 : increase by 5%; If Brake > 0 : increase by 5%
> 3000	Approximates straight line	No correction

It should be emphasized that nonzero preprocessing ratios in multiple channels do not mean that traction and braking are necessarily applied simultaneously as final commands. In the calculation, the final output of each channel is obtained by scaling these ratios with the currently available channel capacity. Therefore, if a given channel provides zero available force at the current speed or operating

state, its final output remains zero after scaling. A further reason for retaining nonzero traction and braking ratios simultaneously is that, in a mild downhill section, both channels may need to remain available for different operating demands. If the current operating condition requires deceleration, the final traction output can still be zero after scaling, even when its baseline ratio is nonzero. Conversely, if the trains are running on a downhill section but the inter-train spacing is gradually increasing and the following train needs to catch up, some traction output may still be required. In this case, retaining a nonzero traction ratio helps preserve control flexibility for the subsequent allocation.

In the present simulation, these preprocessing rules are applied point by point along the breakpoint-based track table, producing $\eta_T(s)$, $\eta_R(s)$, and $\eta_M(s)$ of the whole line, together with the corresponding preallocated-force profiles. These results are then written directly into the two-train cooperative control model and serve as the basic inputs to the subsequent online control calculation. Therefore, this preprocessing step is not merely a conceptual setup, but an actual component of the simulation framework developed in this study.

4.5.2 Finite-horizon inter-train spacing prediction model

In cooperative train operation, the control decision of the following train depends not only on the current inter-train spacing and relative speed, but also on the relative motion in the short future. If the control reacts only to instantaneous states, the response may lag behind the actual operation or become overly conservative under uncertainty, thereby reducing overall operating efficiency. Therefore, a finite-horizon inter-train spacing prediction model is introduced to provide anticipatory information for the subsequent cooperative control.

The basic idea of this model is to estimate the future evolution of inter-train spacing over a finite prediction horizon τ . Here, τ is a finite future prediction horizon, namely the look-ahead time window over which the future spacing is extrapolated from the current states. Within this horizon, the accelerations of the two trains are assumed to remain constant. On this basis, the future spacing

can be predicted from the current positions, speeds, and accelerations, and then used to assess whether the future safety margin remains acceptable.

Let the positions, speeds, and accelerations of train 1 and train 2 at time t be (s_1, v_1, a_1) and (s_2, v_2, a_2) , respectively. The inter-train spacing is defined as

$$g(t) = s_1(t) - s_2(t) \quad (4.19)$$

Under the constant acceleration assumption, the predicted positions at time $t + \tau$ are given by

$$\begin{cases} s_1(t + \tau) = s_1(t) + v_1(t)\tau + \frac{1}{2}a_1(t)\tau^2 \\ s_2(t + \tau) = s_2(t) + v_2(t)\tau + \frac{1}{2}a_2(t)\tau^2 \end{cases} \quad (4.20)$$

Accordingly, the predicted inter-train spacing at time $t + \tau$ can be written as

$$g(t + \tau) = g(t) + (v_1 - v_2)\tau + \frac{1}{2}(a_1 - a_2)\tau^2 \quad (4.21)$$

The equation above provides a short-term estimate of the future inter-train spacing over the finite prediction horizon. If the prediction indicates that the spacing may decrease excessively within the horizon τ , the cooperative control can reduce traction or strengthen braking in advance, thereby improving anticipatory safety regulation.

The choice of the prediction horizon τ should balance two requirements. On the one hand, it must be long enough to capture potentially unsafe spacing evolution in advance. On the other hand, it should not be excessively long, otherwise the prediction may accumulate unnecessary error and make the control strategy overly conservative. Based on the characteristics of the train in different speed ranges, a piecewise definition of τ is adopted. When the speed is below 50 km/h, a shorter prediction horizon of $\tau = 8$ s is used, since the braking distance is relatively short and the system response is faster. When the speed exceeds 50 km/h, a longer prediction horizon of $\tau = 15$ s is adopted to account for the larger inertia and braking demand at higher speed.

4.5.3 Predictive safety control mechanism

In cooperative train operation, changes in the leader train motion or track conditions may cause the inter-train spacing to decrease rapidly. Because the following train cannot respond instantaneously to such changes due to communication, computation, and actuation delays, a predictive safety control mechanism is introduced on top of the finite-horizon inter-train spacing prediction model. The purpose of this mechanism is to convert the requirement that the future spacing must not fall below the prescribed safety distance into an explicit constraint on the admissible acceleration of the following train.

To ensure that the inter-train spacing at the future time $t + \tau$ does not fall below the minimum safety distance s_{\min} , the predicted spacing must satisfy

$$g(t + \tau) \geq s_{\min} \quad (4.22)$$

Substituting the predicted spacing expression from Eq.(4.21) into this constraint gives

$$g(t) + (v_1 - v_2)\tau + \frac{1}{2}(a_1 - a_2)\tau^2 \geq s_{\min} \quad (4.23)$$

Rearranging the above inequality yields the admissible upper bound of the acceleration of the following train,

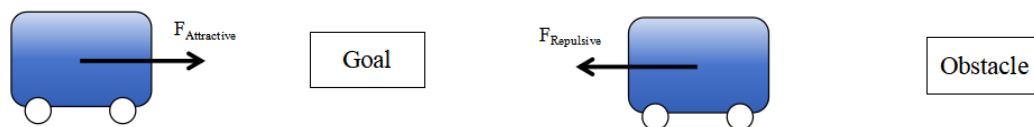
$$a_{2,\max}^{\text{safe}} = a_1 + \frac{2}{\tau^2} [g(t) - s_{\min} + (v_1 - v_2)\tau] \quad (4.24)$$

where $a_{2,\max}^{\text{safe}}$ is the maximum allowable acceleration of the following train under the predictive safety constraint.

Accordingly, when the control computes the traction or braking command of the following train, the resulting target acceleration must not exceed this bound. In this way, the predicted inter-train spacing over the horizon τ is guaranteed to remain no smaller than the prescribed safety distance s_{\min} , so that the safety constraint acts in an anticipatory manner rather than only after the spacing has already become critically small.

4.5.4 Velocity-based artificial potential field control

The artificial potential field (APF) approach was originally developed for robotic path planning and obstacle avoidance. The main idea is to construct an attractive potential field around the target point and repulsive potential fields around obstacles. When the controlled agent moves within the resultant field, it is simultaneously subject to attractive and repulsive forces, and the direction of their resultant indicates a safe and efficient motion trend. As shown in Figure 4.9, the attractive force dominates when the agent is far from the target, while the repulsive force increases sharply as it approaches an obstacle, steering it away from potential collision regions. Owing to its simple structure and low computational burden, the APF method has been widely applied to multi-agent obstacle avoidance, cooperative control and trajectory-keeping problems.



(a) Illustration of the attractive force (b) Illustration of the repulsive force

Figure 4.9 Illustration of attractive and repulsive forces acting on the agent during motion

In cooperative train operation, the APF concept can be used to handle the dynamic train-following relationship between the leader and following trains. The leader train is treated as the target, the following train as the controlled agent, and the combined effect of their relative speed and inter-train spacing determines the direction and magnitude of the potential field. When the leader train runs faster or the inter-train spacing becomes too large, the attractive field is strengthened and encourages the following train to accelerate and close the gap; when the inter-train spacing is too small or the following train is too fast, the repulsive field dominates, suppressing further acceleration and promoting braking. The superposition of the two fields yields a composite potential field, allowing the following train to realize stable train-following behavior around a dynamic safety spacing.

To make the control process consistent with the continuity and physical constraints of railway systems, a velocity-based APF model is adopted, in which the APF output acceleration a_{APF} is formulated as a nonlinear function of the speed difference between the two trains and the integral error of this speed signal. Assuming that at time t the speeds of the leader and following trains are $v_1(t)$ and $v_2(t)$, respectively. The instantaneous speed difference between the two trains is then defined as

$$\Delta v(t) = v_1(t) - v_2(t) \quad (4.25)$$

To capture the accumulated effect of their relative motion over time, an integral of the speed difference is introduced:

$$h(t) = \int_0^t \Delta v(\tau) d\tau \quad (4.26)$$

where $h(t)$ is an integrated speed-difference term that serves as a spacing-related variable, replacing the direct use of inter-train spacing as the control input. In the numerical implementation, $h(t)$ is updated by discrete-time integration and is limited within a prescribed range to suppress long-term drift of the integral.

During train-following, the safety interval should vary with speed. To this end, a desired spacing-related reference linked to the speed of the leader train is introduced as

$$s_{\text{ref}}(t) = s_0 + T_{\text{bias}} v_1(t) \quad (4.27)$$

Where s_0 is the minimum interval offset at low speed or standstill, and T_{bias} is a safety time-interval parameter that represents the additional interval required as speed increases. Based on these definitions, the error of the spacing-related variable is written as

$$e_h(t) = h(t) - s_{\text{ref}}(t) = h(t) - (s_0 + T_{\text{bias}} v_1(t)) \quad (4.28)$$

When $e_h(t) > 0$, the spacing-related variable is larger than desired; when $e_h(t) < 0$, the interval is insufficient. The control law must adapt the acceleration of the following train differently in these two cases. However, using only $e_h(t)$ would overlook the current trend of the relative speed, whereas

relying solely on the instantaneous speed difference would not capture the long-term behavior of the integrated interval. To account for both aspects, the speed difference and the spacing-related-variable error are linearly combined into a single potential-field variable:

$$\xi(t) = \alpha\Delta v(t) + \beta e_h(t) \quad (4.29)$$

Where α and β are weighting coefficients that balance the relative influence of the instantaneous speed difference and the spacing-related-variable error in the controller. By tuning α and β , a trade-off can be achieved between convergence speed and stability of the spacing-related variable.

Within the APF framework, this combined term can be regarded as a one-dimensional potential-field variable that measures how far the system deviates from the desired train-following state. To obtain an acceleration command that is smooth and bounded in magnitude, the hyperbolic tangent function $\tanh(\cdot)$ is used to map the potential-field variable in a nonlinear way, leading to the following velocity-based APF acceleration control law:

$$a_{APF}(t) = k_a \tanh(\xi(t)) = k_a \tanh(\alpha\Delta v(t) + \beta e_h(t)) \quad (4.30)$$

where k_a is a gain determining the amplitude of the acceleration, that is, the maximum adjustment strength of the controller in the saturation region of the potential field.

When $\alpha\Delta v(t) + \beta e_h(t)$ is close to zero, $\tanh(\cdot)$ behaves almost linearly and $a_{APF}(t)$ responds approximately linearly, which is favourable for smooth fine-tuning around the desired spacing-related reference. When $\alpha\Delta v(t) + \beta e_h(t)$ has a large absolute value, $\tanh(\cdot)$ saturates naturally, and $|a_{APF}(t)|$ is limited to $|k_a|$, thus preventing excessively large acceleration or deceleration commands.

In practical operation, the $a_{APF}(t)$ cannot be used directly, and it must be combined with the predictive safety constraint to ensure that the following train does not approach the leader too aggressively or even collide with it.

$$a_2(t) = \min \{ a_{\text{APF}}(t), a_{2,\text{max}}^{\text{safe}}(t) \} \quad (4.31)$$

For a given admissible acceleration, the required net traction force is

$$F_{\text{net}}(t) = m_{\text{eff}} a_2(t) \quad (4.32)$$

where m_{eq} is the equivalent train mass, which accounts for the rotational inertia of wheels and drivetrain components as an added mass so that the dynamics can be represented with a single mass parameter. The net traction force is obtained as the difference between the traction force and the total braking force:

$$F_{\text{net}}(t) = F_T(t) - [F_R(t) + F_M(t)] \quad (4.33)$$

where F_T , F_R and F_M denote the traction force, regenerative braking force and mechanical braking force, respectively. Each of these forces is determined by its corresponding maximum available force and the percentage allocation coefficients:

$$\begin{aligned} F_T(t) &= \gamma_T(t) F_{T,\text{max}}(v_2(t)) \\ F_R(t) &= \gamma_R(t) F_{R,\text{max}}(v_2(t)) \\ F_M(t) &= \gamma_M(t) F_{M,\text{max}}(v_2(t)) \end{aligned} \quad (4.34)$$

$$0 \leq \gamma_T(t), \gamma_R(t), \gamma_M(t) \leq 1 \quad (4.35)$$

During control, the percentage coefficients are adjusted so that equation (4.33) satisfies the following relationship:

$$F_T(t) - [F_R(t) + F_M(t)] \approx m_{\text{eff}} a_2(t) \quad (4.36)$$

In this way, under the predictive safety constraint, the desired acceleration generated by the artificial potential field is mapped to concrete traction and braking allocations, so that stable train-following is achieved in the vicinity of the dynamic safety distance.

The artificial potential field function based on speed difference is shown in Figure 4.10. When $\Delta v < 0$, the potential field operates in the repulsive region and the system generates a negative acceleration to mitigate rear-end risk;

when $\Delta v > 0$, it lies in the attractive region and the system produces a positive acceleration to let the following train catch up with the leader.

The corresponding potential-energy distribution is given in Figure 4.11. As the speed difference between the two trains approaches zero, the potential-energy function reaches its minimum and the system settles at a stable equilibrium, indicating that the trains maintain a safe spacing with matched speeds.

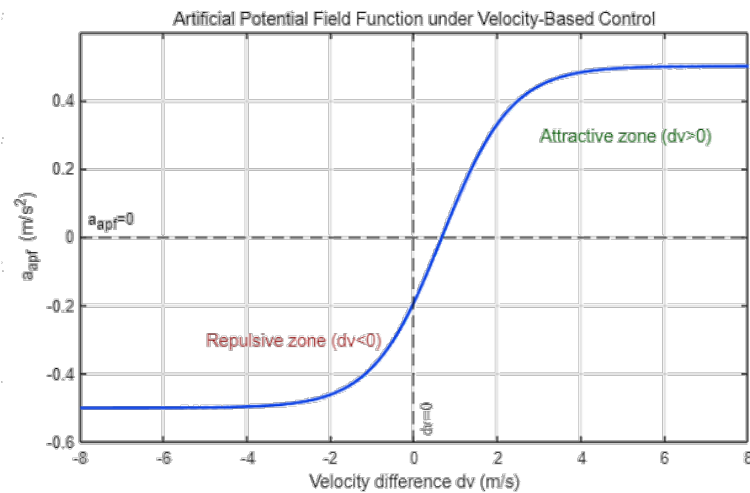


Figure 4.10 Artificial potential field function curve based on speed difference

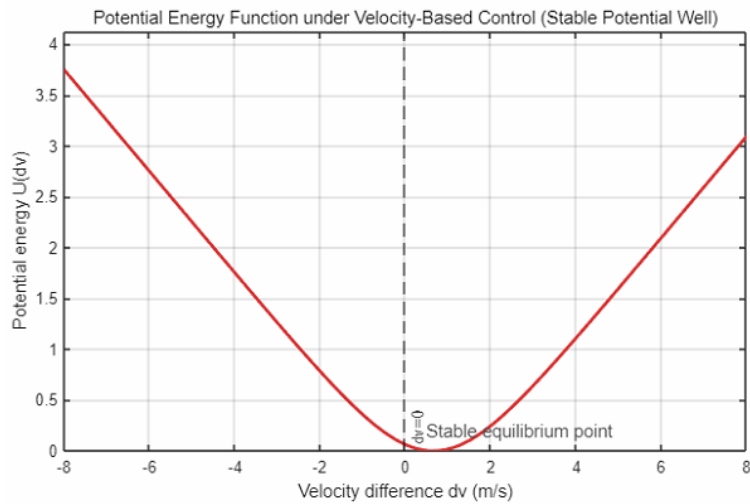


Figure 4.11 Potential energy distribution

4.5.5 Stopping and restart control

(1) Stopping

During operation, the stopping control of the following train must be determined from its current speed, remaining distance and track conditions, when to initiate braking and with what braking intensity to decelerate to zero. To avoid efficiency loss due to overly early braking, and insufficient safety spacing due to delayed braking, a dynamic stopping trigger based on real-time distance and speed is adopted, combined with the braking curve to achieve smooth deceleration. Here, the stopping trigger refers to the decision logic that determines whether the train should enter the braking phase according to the current situation.

When the train approaches a predefined stop point, the system computes the theoretical braking distance from the current speed v , as given by

$$s_{\text{req}} = \frac{v^2}{2a_{\text{brake}}(v)} \quad (4.37)$$

Where $a_{\text{brake}}(v)$ is obtained by interpolation from the braking characteristic curve, representing the maximum effective deceleration that can be achieved at that speed. At the same time, the actual remaining distance from the current position to the next stop point is calculated as in equation:

$$d_{\text{stop}} = s_{\text{stop}} - s \quad (4.38)$$

The stopping trigger condition is therefore defined by equation:

$$0 \leq d_{\text{stop}} \leq s_{\text{req}} + s_{\text{buffer}} \quad (4.39)$$

Where s_{buffer} provides additional margin to prevent abrupt deceleration or stopping too close to the target point.

Once the braking phase begins, the traction force is forced to zero, and the train decelerates progressively with regenerative braking as the primary means and mechanical braking as a supplement. The share of regenerative braking is set as high as possible to maximize energy recovery, while the proportion of mechanical braking is adjusted according to the gradient of the track to compensate braking demand under different operating conditions. As the speed gradually decreases, the stop is considered complete when the train speed

reaches 0 km/h, thereby realizing a smooth and controlled soft-stopping process. The stopping trigger and active braking region are illustrated in Figure 4.12, and the time evolution of the speeds of the leader and following trains is shown in Figure 4.13.

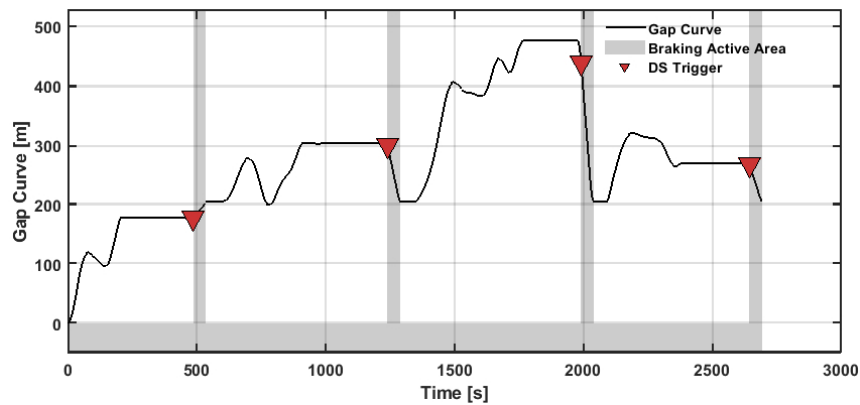


Figure 4.12 Illustration of stopping trigger and active braking spacing

In Figure 4.12, the black solid line represents the actual instantaneous inter-train spacing between two trains, the grey shaded regions indicate the periods when braking is active, and the triangular markers are the stopping trigger points. The clear temporal correspondence between the trigger points and the following braking intervals over multiple stop cycles shows that the stopping mechanism determines the onset of braking in advance, rather than merely reacting passively after the spacing has already decreased. Moreover, no spike-like or abrupt shrinkage of the inter-train spacing is observed in the vicinity of the trigger points. Instead, the spacing evolves smoothly throughout the braking phases, and no chattering or oscillatory behavior caused by repeated braking activation is evident. This indicates that the stopping trigger mechanism provides stable and well-timed braking initiation, thereby ensuring the temporal stability of the stopping control.

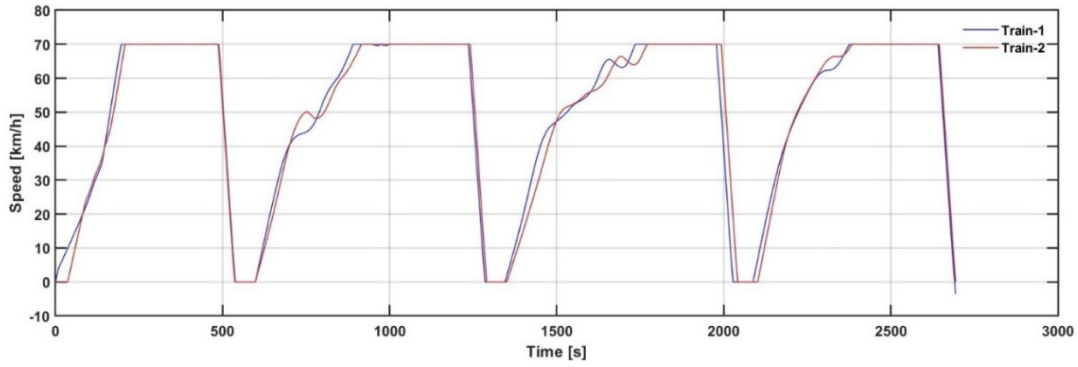


Figure 4.13 Comparison of leader and following train speeds over time

As shown in Figure 4.13, the speed of Train-2 exhibits a continuous and smooth decrease around each stopping point and quickly matches the speed of Train-1, achieving synchronous stopping. This indicates that, under the imposed safety constraints, the braking control strategy ensures a stable and well-coordinated stopping behavior.

(2) Restart

After the stopping phase, the train enters a dwelling and waiting stage. To avoid unintended departures caused by communication delay, incomplete departure of the leader train, or unsatisfied track conditions, the system must incorporate an adaptive restart control mechanism. During dwelling, the train keeps its speed at zero while continuously monitoring the speed and position of the Train-1, as well as their dynamic relative motion. Accordingly, the system computes the integral of the speed difference from the stopping time to the current time:

$$e_v(t) = \int_{t_{\text{stop}}}^t (v_1(\tau) - v_2(\tau)) d\tau \quad (4.40)$$

This quantity is used as a measure of how much the spacing has recovered, and represents the effective relative displacement between the following and leader trains. Once $e_v(t)$ satisfies a prescribed restart condition, the system regards the departure criteria as fulfilled and initiates the restart process.

(a) Train-1 has already started ($v_1(t) > 0$), Train-2 has been dwelling for 30s, and the integral of the speed difference has reached the threshold associated with the safe spacing ($e_v(t) \geq 0.9 s_{\text{safe}}$).

(b) Train-1 has already started ($v_1(t) > 0$), and Train-2 has been dwelling for 60s.

The restart criterion and the recovery process of the safe spacing are illustrated in Figure 4.14. When the integral of the speed difference $e_v(t)$ gradually recovers over time and exceeds 90% of the safe spacing $s_{\text{safe}}(t)$, the system judges that an effective relative spacing between two trains has been re-established. Therefore, if the minimum dwelling time requirement is also satisfied, the train enters the restart phase, enabling a safe and smooth departure control.

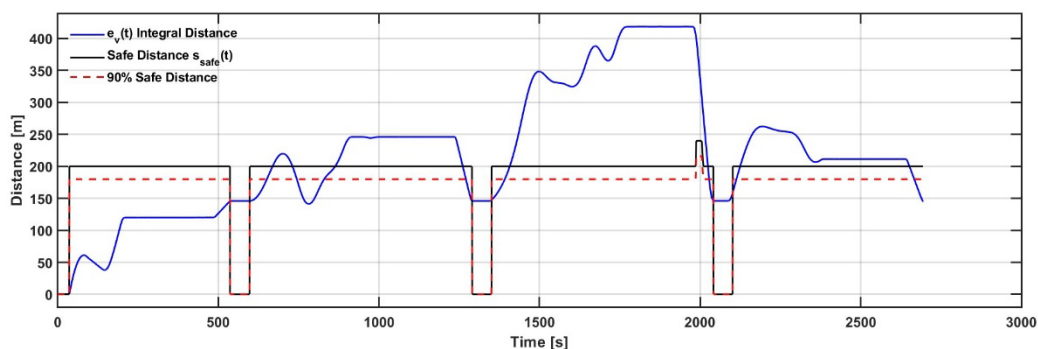


Figure 4.14 Illustration of restart criterion and recovery of safe spacing

The restart control mechanism works in coordination with the stopping mechanism and together they form a complete start–stop logic for the trains. By imposing constraints on both spacing recovery and minimum dwelling time, the mechanism provides safety redundancy, so that operational reliability is maintained even under communication disturbances or delayed departure of the leader train. At the same time, the combined use of the integral of the speed difference and the safe distance enables smooth reconnection with the leader train and adaptive adjustment of the spacing.

4.6 Case study setup and description

4.6.1 Train

In the following case study, a typical heavy-haul iron-ore train operated by LKAB on the Iron Ore Line/Ofoten Line in Sweden is used as the reference case. The train consists of two IORE electric locomotives and 68 hopper wagons, with a gross train mass of about 8600 t, an overall length of roughly 750m, and an axle load of approximately 30t, which makes it representative of a typical long and heavy freight train. The detailed parameters are listed in Table 4.4.

Table 4.4 The main parameters of the train [44]

Parameter	IORE (2 sections)	Fanoo	Train
Length (between couplers) [m]	45.8	10.3	746.2
Tare mass [t]	360	21.6	1828.8
Cargo load (STAX 30) [t]	0	98.4	6691.2
Gross mass (STAX 30) [t]	360	120	8520
Adhesive weight [t]	360	0	360
Mass contribution (rotational masses) [t]	52	1.64	163.52
Braked weight [t]	280	48	3544



Figure 4.15 IORE locomotive section [44]



Figure 4.16 Fanoo iron ore wagon [44]

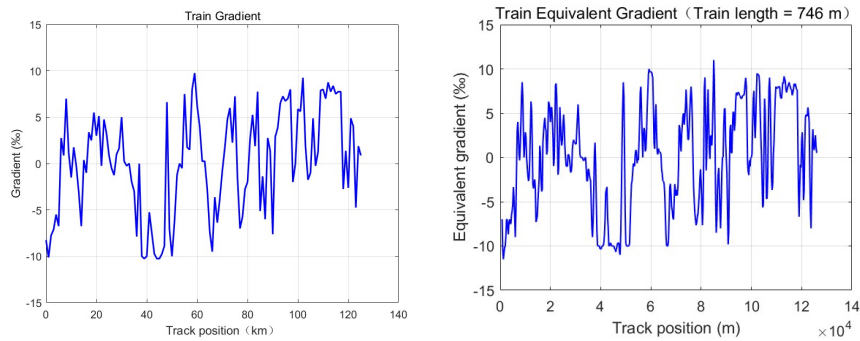
The train is powered by two coupled IORE electric locomotives, and the speed-dependent traction and braking curves have been presented in Section 4.2. It should be noted that these curves already account for engineering constraints such as wheel–rail adhesion, locomotive rated power, and electric braking capability. Therefore, the adhesion limit $F \leq \mu_{adh}mg$ is not introduced separately in this study, and the train is assumed to operate under nominal dry-rail conditions. The running resistance has likewise been included in the unified longitudinal dynamics model of Section 4.2.

4.6.2 Track

The case study is based on a standard operating segment of the Kiruna-Narvik heavy-haul railway used by LKAB for iron-ore transport. Daily scheduling and maintenance are carried out by LKAB’s operating subsidiary. The line passes through highly undulating terrain with long gradients, short steep ramps, and numerous curves and tunnels, making it a representative mountainous heavy-haul freight corridor with strict requirements on traction capability and longitudinal dynamic performance.

The track geometry and operating condition data used in this study are consistent with the referenced work and originate from the same measured/design database [44]. The raw track data are provided in terms of mileage breakpoints, where each breakpoint stores the location, gradient, curve radius, speed limit, station position and related attributes. These records form the basis for computing the equivalent curve radius and equivalent gradient.

The detailed procedure for the equivalent treatment of track geometry has been presented in Section 4.1. Figure 4.17 shows the measured profile over the full operating section of approximately 126 km, together with the corresponding processed equivalent gradient profile.



(a) The measured gradient profile (b) The equivalent gradient profile

Figure 4.17 The gradient profile of the whole 126 km

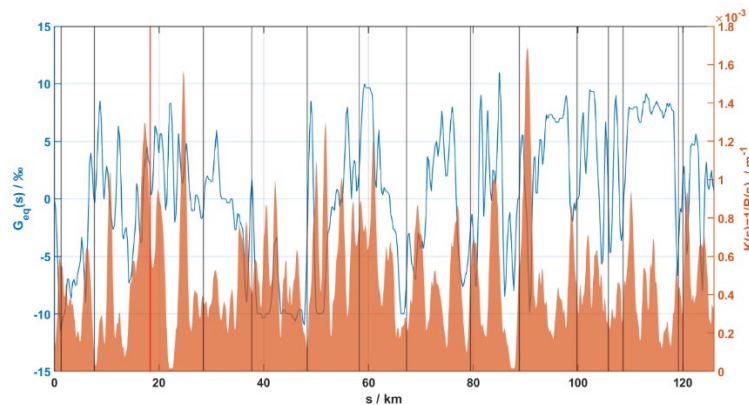


Figure 4.18 Equivalent gradient, equivalent curve-radius distribution, and stopping-point locations of the whole 126 km

The original track data span approximately 126 km of the full operating section. However, the simulation itself is not performed over the entire line. Because a small step length is used for track discretization (with breakpoint spacing reduced to the order of a few meters after preprocessing), a full 126km simulation would lead to a substantial increase in computational load and output data volume, without bringing proportional benefit to the comparison of control strategies. Moreover, from the viewpoint of scenario representativeness, it is unnecessary to include the whole line in order to capture the main

operating regimes of heavy-haul trains. Therefore, this study selects only the first four stations from the origin station as the simulation domain, with a total track length of about 37.7 km.

This section includes several typical operating conditions, including start-up acceleration, cruising, passing through speed-restricted curves, braking for station entry, and stopping. It also contains various combinations of gradients and curves. In this way, the simulation scale and computational burden are significantly reduced while still preserving sufficiently rich track features within a limited distance, thereby providing a representative scenario for the subsequent comparison and evaluation of VC control strategies.

4.6.3 Representative simulation scenario and control activation timeline

Based on the train and track data described above, a representative simulation scenario is constructed to examine how the cooperative control framework established in Section 4.5 operates under the given case inputs.

The dynamic evolution of the inter-train spacing and the activation phases of the different control strategies are shown in Figure 4.19, including Dynamic stopping (DS) active, APF accel, APF brake, Predictive safety clamp, Pre-limit deceleration, and the Restart window. In addition, the grey inverted triangles indicate the Dynamic stopping trigger, and the green triangles denote Restart.

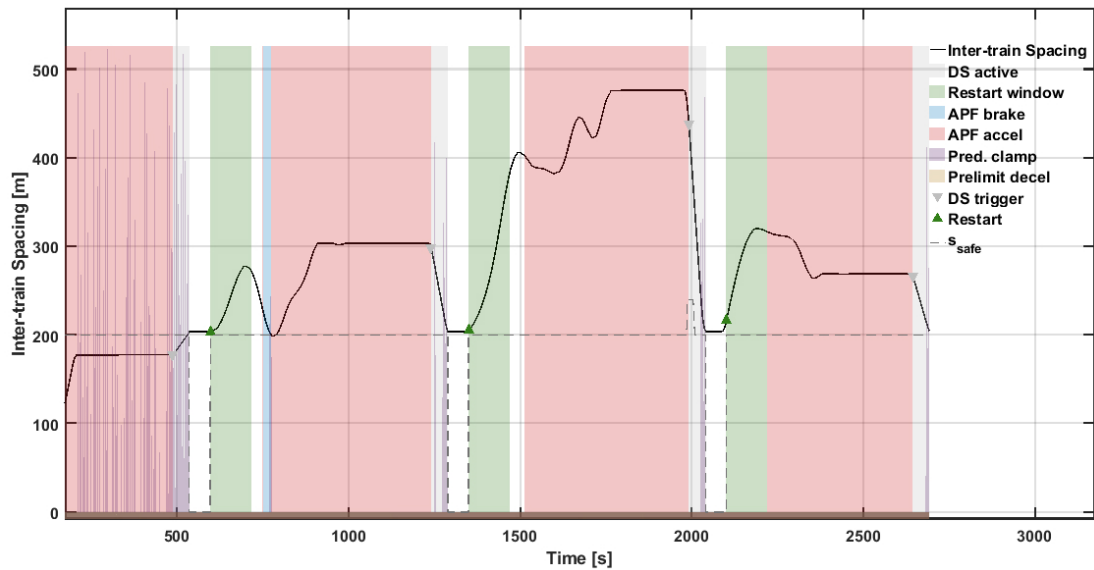


Figure 4.19 Time history of inter-train spacing and control activation phases in the representative simulation scenario

In the initial start-up phase (0–487 s), the inter-train spacing is almost zero and far below the safety threshold, so the system classifies this as a high-risk period, highlighted by the light-grey background (DS active). Because of the extremely small spacing and large speed difference, the APF module switches frequently between attractive and repulsive actions, shown by the alternating red (APF accel) and blue (APF brake) bands, to regulate the speed difference while preventing further spacing reduction. At the same time, the predictive safety clamp is repeatedly activated, as indicated by the purple bands (Pred. clamp), to softly limit the traction output whenever the predicted future spacing becomes insufficient.

After this initial phase, the system repeatedly undergoes three-time dynamic stop–dwell–restart cycles (487–598 s, 1241–1350 s and 1992–2101 s). In operation, train 2 reaches the dynamic stopping point (grey inverted triangles, DS trigger) and simultaneously enters the light-grey region (DS active). The traction force is then cut off, while regenerative and mechanical braking are allocated adaptively according to the gradient, yielding controlled deceleration until the speed reaches zero. During deceleration, whenever the prediction model indicates that the future interval may approach or fall below the safety

limit, purple bands (Pred. clamp) appear intermittently, applying additional soft clamping on the net traction to prevent overshoot before the stop.

Once the train has come to a complete stop, it enters a dwelling state. During this period, both APF control and predictive clamping are temporarily disabled, and the spacing remains approximately constant around the safety threshold. When the minimum dwelling time has been satisfied and the restart criterion is fulfilled, the restart phase begins. In the figure this is indicated by green vertical bands (Restart window) and green triangle markers (Restart). At this point, the traction channel is gradually restored, and the train accelerates back into the next following phase.

In the intervals 598–1241 s, 1350–1992 s and 2101–2644 s, the trains operate in the normal following phase between a restart and the next dynamic stop. Each restart is indicated by a green vertical band (Restart window) and a green triangle (Restart), after which the system enters a safe running region dominated by the light-grey background (DS active). Dynamic stopping protection remains enabled but no longer enforces deceleration; it acts only as a global safety constraint. During this stage, longitudinal control is mainly governed by the combined action of the APF and the predictive safety module. After each restart, the spacing is usually close to the safety threshold and the speed of the following train is relatively low, so the attractive mode of the APF is activated, appearing as red bands (APF accel) that drive train 2 to accelerate. When the speed difference reverses sign or the integrated interval becomes too small, the APF switches to the repulsive mode, shown as blue bands (APF brake), to suppress overshoot. If the prediction model indicates that the future interval may be insufficient, purple bands (Pred. clamp) are triggered to soften the APF-induced acceleration and tighten the safety margin. Meanwhile, the brown band at the bottom (Prelimit decel) adjusts the upper speed bound in advance according to speed limits and gradients, preventing potential overspeed during the closing process.

In the final stopping phase from 2644–2694 s, the trains gradually approach the terminal stopping position. When train 2 reaches the last braking point

computed by the system, grey inverted triangles (DS trigger) appear in the figure and train 2 enters the dynamic stopping state indicated by the light-grey background (DS active). The traction channel is closed, and regenerative and mechanical braking are allocated as required to achieve controlled deceleration. During this phase, the prediction model indicates that the future interval may become insufficient, which is shown as purple vertical bands (Pred. clamp) that further constrain the traction and braking outputs through soft clamping and prevent overshoot before the final stop. Through the coordinated action of the different mechanisms, the last stopping process remains smooth and controllable, and train 2 eventually stops at about 200 m behind the leader train.

The proposed multi-strategy cooperative control framework exhibits good feasibility and consistency throughout the entire run. The APF provides real-time regulation of the speed difference, the predictive safety clamp offers forward-looking constraints, dynamic stopping guarantees enforced braking under extreme conditions, and the pre-limit module adjusts the upper speed bound in advance. Each mechanism plays a distinct role while complementing the others, enabling the system to maintain a safe inter-train spacing and prevent overshoot in all phases, thereby demonstrating the effectiveness and robustness of the designed control strategy.

4.7 Summary

This chapter established the longitudinal dynamics and cooperative control strategy for VC train operation. Under clearly stated modelling assumptions, a unified longitudinal dynamics model was developed for the heavy-haul train, including traction, braking, running resistance, gradient resistance, and curve resistance. To account for the train-length effect while retaining the simplicity of the single-point dynamics framework, an equivalent treatment of track geometry was introduced, through which the horizontal alignment data and vertical profile data were transformed into the equivalent curve radius and equivalent gradient.

On this basis, a time-domain description for the two trains was constructed, and communication and actuation delays were represented as equivalent spatial lag within the breakpoint-based track framework. These treatments enabled the model to incorporate train data, track data, and delay effects in a consistent manner under realistic operating conditions.

Building on the above framework, an integrated cooperative control strategy was developed for the following train. As defined in Section 4.5, this driving strategy consists of track-dependent preprocessing rules, a finite-horizon inter-train spacing prediction model, a predictive safety control mechanism, a velocity-based APF control law, and stop-restart control. These modules operate at different levels but in a coordinated manner: preprocessing provides baseline channel allocation, the prediction and predictive safety modules impose anticipatory safety constraints, the APF law generates the main following-control action, and the stop-restart logic handles special operating phases. Together, they allow the following train to adjust its traction and braking actions according to the state of the leader train, the evolution of inter-train spacing, and the track conditions, while maintaining safety and smooth operation.

Finally, the chapter introduced the case study description and setup, including the train data, track data, and a representative simulation scenario for illustrating the activation and coordination of the proposed control strategy. This provides the basis for the result analysis and comparative evaluation of different driving-strategy configurations in the following chapter.

5 Results and discussion

Building on the previously established longitudinal train dynamics framework and cooperative control architecture, this chapter further evaluates the performance of different control strategies through numerical simulations. First, the single-point model and the proposed multi-point model are compared in terms of following performance, speed fluctuation, and inter-train spacing stability, in order to assess how the level of dynamical modeling affects control performance. The chapter then examines how different driving strategy controls influence operational efficiency and safety, and investigates how alternative control functions shape system behavior under the defined control objectives. In addition, sensitivity studies are conducted for key parameters such as start-up delay, maximum allowable acceleration, and initial inter-train spacing, so as to reveal how these factors influence the dynamic coupling between trains. The systematic analysis of these simulation results offers targeted insights for refining control strategy design and assessing the feasibility of engineering implementation.

5.1 Comparative analysis of the single-point model and multi-point model

As mentioned before, in the traditional single-point model, a train is abstracted as a single reference point, so that the influence of train length is neglected. In this study, the proposed multi-point model introduces a sliding-window

equivalent treatment based on train length while retaining the basic structure of the single-point longitudinal dynamics model. A comparative analysis of the single-point model and the proposed multi-point model is carried out, and the results are shown in Figure 5.1.

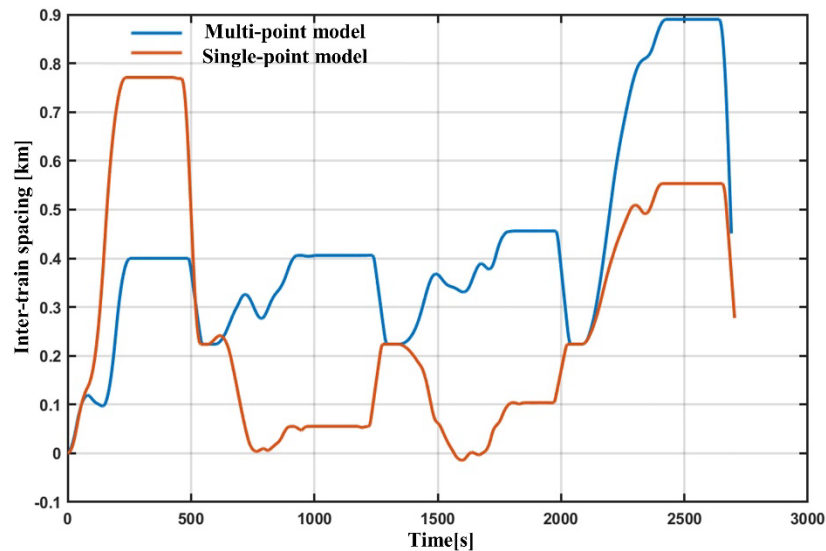


Figure 5.1 Inter-train spacing of single-point model and multi-point model

As illustrated in Figure 5.1, the two models exhibit clear differences in the predicted inter-train spacing. Because the traditional single-point model directly uses original point track inputs, it is more sensitive to abrupt changes in speed limits, gradient, and curve radius, which leads to stronger local fluctuations in the spacing. In sections with pronounced geometric variation, the spacing may even become slightly negative. It should be noted that these values should not be interpreted as physically meaningful negative spacing. Their magnitude is very small (less than 10 m) compared with the total train length of about 746 m, indicating that they are more likely caused by local estimation bias of the single-point approximation in sections with strongly varying track geometry, where train-length effects are neglected.

By contrast, the proposed multi-point model applies the equivalent treatment of track geometry over the train length and therefore better reflects the combined influence of the external conditions acting on different parts of the train. As a

result, its predicted inter-train spacing is more continuous, with smaller artificial fluctuations and without the slight negative values observed in the single-point model. This indicates that the multi-point model can more effectively suppress the local distortion introduced by the simplified point representation and provide a more physically consistent description of relative train motion.

Overall, the proposed multi-point model retains the computational simplicity of the single-point model while significantly improving the physical consistency and stability of inter-train spacing prediction. This makes it more suitable for the subsequent prediction and cooperative control of relative train motion in VC operation.

5.2 Impact of the proposed driving strategy on train operation

Having shown in the previous section that the multi-point model provides a more physically consistent and stable description of train motion, this section further examines how the proposed driving strategy affects cooperative train operation. As defined in Section 4.5, the driving strategy in this thesis refers to the integrated cooperative control framework for the following train. To clarify the role of different control components, three configurations are compared: (1) a baseline case without the proposed driving strategy; (2) a reduced strategy including only track-dependent preprocessing and predictive safety control; and (3) the full driving strategy, in which all control modules are activated. In Figure 5.2 and Table 5.1, these three configurations are labeled as “without using driving strategies”, “using driving strategies (only initial track and predictive safety)”, and “using driving strategies”, respectively. The inter-train spacing curves under these three configurations are shown in Figure 5.2, and the corresponding statistical comparison is summarized in Table 5.1.

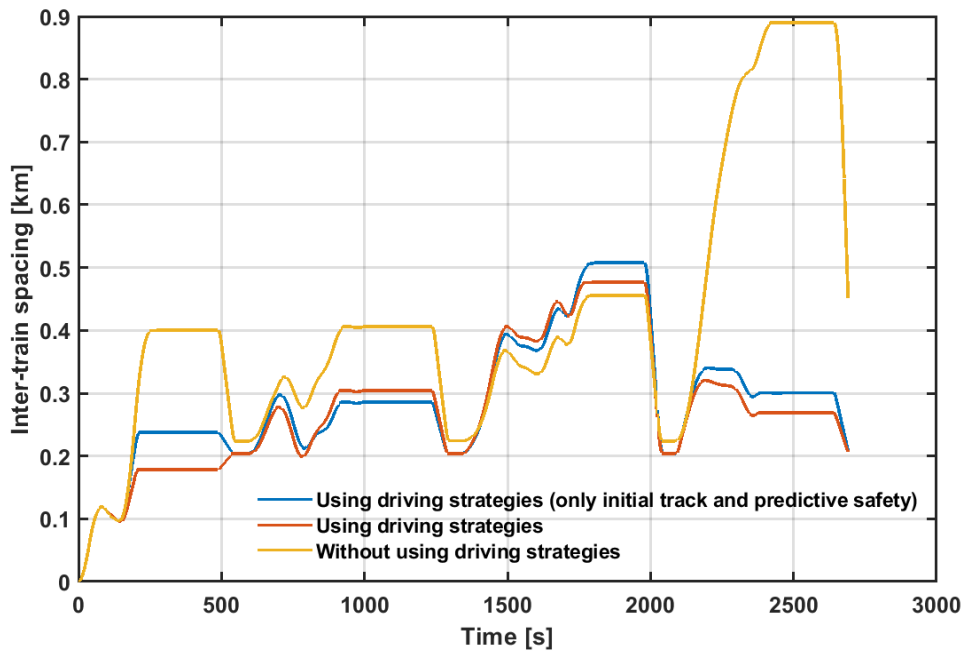


Figure 5.2 Inter-train spacing under three control configurations

Table 5.1 Statistical comparison of inter-train spacing under three control configurations

Control mode	Mean (m)	Standard deviation (m)	Maximum (m)	Minimum (m)
Without driving strategies	418	212	890	224
Using strategies (Initial track + predictive safety)	290	100	507	203
Using full driving strategies	277	101	476	200

As shown in Figure 5.2 and Table 5.1, the inter-train spacing exhibits pronounced fluctuations when no driving strategy is applied. The maximum deviation reaches approximately 0.89 km, with a mean spacing of 418 m and a standard deviation as high as 212 m. This indicates that the following train has difficulty maintaining stable following under the leader train's speed disturbances, and the overall system behaves passively.

After introducing the initial trajectory planning and predictive safety control, the spacing fluctuations become noticeably smaller. The mean spacing

decreases to 290 m, and the standard deviation is reduced to about 100 m. This indicates that the predictive safety constraint effectively suppresses abrupt variations in inter-train spacing and improves the dynamic response of the following process.

When using the full driving strategy control, the performance improves further. The mean spacing decreases to 277 m, corresponding to a reduction of approximately 33.7% relative to the case without driving strategy. The standard deviation remains around 101 m, which is about 52.4% lower than that of the no-strategy case, indicating a substantial improvement in the stability of the following process. Meanwhile, the maximum spacing is kept below 476 m, and the minimum spacing remains close to 200 m, showing that the system maintains the spacing within a relatively compact and safe range. The spacing histories further show that the full strategy produces the smoothest operation, with almost no large peaks or deep troughs. The overall simulation suggests that the strategy can effectively suppress spacing oscillations caused by the acceleration and deceleration of the leader train, thereby improving the robustness, safety, and smoothness of train following.

5.3 Effects of different control function formulations on train operation

The effectiveness of cooperative train control depends not only on the selected control strategy but also on the intrinsic form of the control function itself. Different control functions exhibit distinct response characteristics when processing spacing difference, speed difference, and acceleration difference. These characteristics directly influence following stability, following speed, and the overall smoothness of train operation. To systematically assess how control function formulations influence train-following performance, this section compares several representative linear control functions with the nonlinear artificial potential field (APF) control function based on speed difference.

Before discussing the results, a brief description of these control functions is given. Here, control function refers to the mathematical mapping from the selected feedback variables to the commanded control output. Distance

feedback, speed feedback, and acceleration feedback all belong to difference-based linear feedback control, distinguished by the state variables they employ:

- (1) Distance-feedback control generates commands solely from the spacing difference. Its structure is simple, but it is more sensitive to disturbances.
- (2) Speed-feedback control adjusts the commanded acceleration according to the speed difference, enabling the system to anticipate and track the motion trend of the leader train.
- (3) Acceleration-feedback control further improves responsiveness to changes in the acceleration and deceleration of the leader train, making the control action more anticipatory.

The combination of these three feedback terms forms a three-parameter feedback structure, whose mathematical form is given by

$$u = K_s \cdot e_s + K_v \cdot e_v + K_a \cdot e_a \quad (5.1)$$

where e_s is the spacing difference, representing the deviation of the current inter-train spacing from the desired safety spacing. e_v is the speed difference between the leader train and the following train. e_a is the acceleration difference, representing the discrepancy between their acceleration or deceleration trends. K_s , K_v , and K_a are the corresponding feedback gains. Equation above (5.1) therefore represents a weighted linear combination of spacing, speed, and acceleration differences.

Unlike the linear control functions described above, the APF control adopts a nonlinear regulation structure, mapping the speed difference continuously through an attraction and repulsion mechanism.

The inter-train spacing histories under different control functions are compared in Figure 5.3, and the corresponding statistical results are listed in Table 5.2.

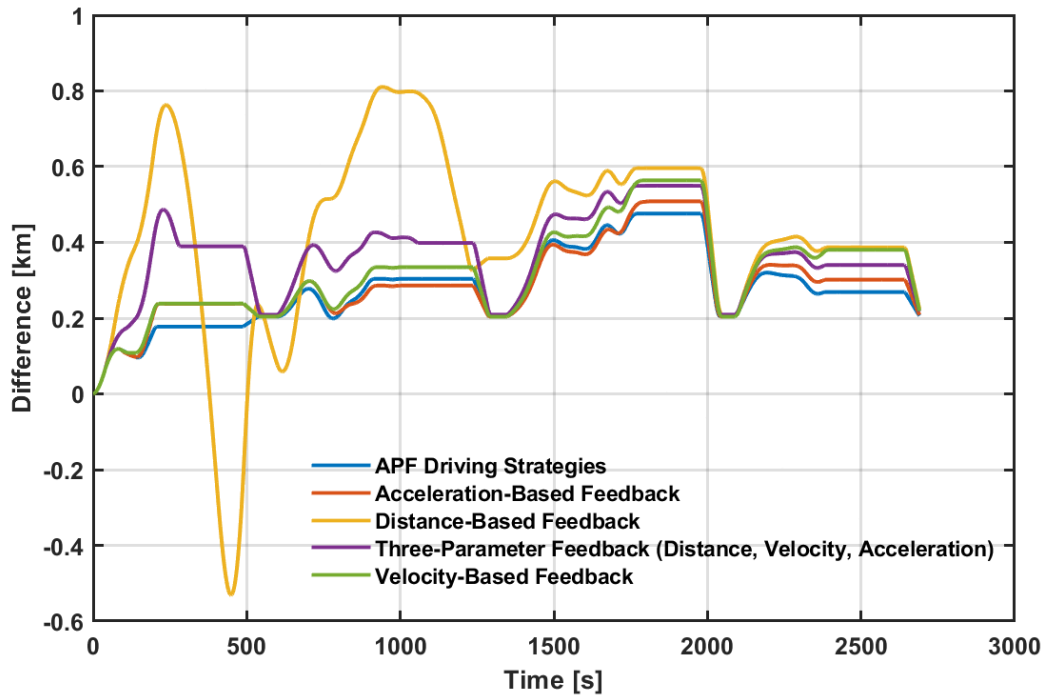


Figure 5.3 Inter-train spacing histories under different control functions

Table 5.2 Statistical comparison of inter-train spacing under different control functions

Control Mode	Mean (m)	Standard deviation (m)
Distance-based feedback	422	250
Velocity-based feedback	323	119
Acceleration-based feedback	291	100
Three-parameter feedback	365	109
APF driving strategies	277	101

As shown in Figure 5.3, different control functions produce clearly different spacing responses. Distance-feedback control is the most sensitive to disturbances, and the spacing even becomes negative over part of the trajectory. These negative values should not be interpreted as physically meaningful spacing. Instead, they indicate that, under the present gains and test scenario, distance-feedback control used alone fails to maintain a feasible and safe following state. In other words, the control does not provide sufficient dynamic damping to cope with the leader train’s speed changes, and the resulting spacing response loses physical admissibility.

By contrast, speed-feedback control and acceleration-feedback control are both significantly more stable, they can better decrease disturbances caused by the leader train. Their spacing histories gradually converge as time progresses, indicating effective suppression of oscillatory behavior. Among the two, acceleration-feedback control gives the smallest standard deviation (100 m), slightly lower than that of speed-feedback control (119 m), suggesting that explicit use of acceleration difference improves responsiveness to changes in the leader train's motion.

Although the three-parameter feedback control incorporates more state information, its performance is not uniformly better. The spacing history still shows noticeable mid-frequency oscillations, and its standard deviation (109 m) remains higher than that of acceleration-feedback control. This suggests that adding more feedback terms does not automatically improve performance; if the gain interaction is not properly balanced, the coupling among feedback terms may instead introduce additional oscillatory behavior.

The APF control function exhibits the smoothest spacing. Its spacing history remains well bounded throughout acceleration, deceleration, and cruising phases, without the pronounced oscillations observed in distance-feedback control or the visible mid-frequency fluctuations present in the three-parameter linear case. Owing to the saturation property of the nonlinear APF function, the commanded acceleration naturally weakens as the state approaches equilibrium, thereby reducing repeated over-correction and limiting overshoot. In terms of statistical indicators, the standard deviation of APF control (101 m) is essentially the same as that of acceleration-feedback control, while its mean spacing (277 m) is the lowest among the compared methods.

Table 5.2 supports the same conclusion. Distance-feedback control performs worst, with the largest standard deviation (250 m) and the appearance of negative spacing values, indicating poor following reliability. Speed-feedback and acceleration-feedback control both achieve much smaller spacing fluctuations, with acceleration-feedback giving the best performance among the linear control functions. The three-parameter feedback control remains

intermediate: it performs better than distance-feedback control, but does not surpass the simpler acceleration-feedback function. APF control does not produce the numerically smallest standard deviation, but it provides the most balanced overall behavior by combining low fluctuation, bounded response, and smooth temporal evolution.

In summary, the comparison shows that the control function has a strong influence on train-following performance, and the nonlinear APF control offers the most balanced overall response, owing to its smooth attraction-repulsion mechanism and inherent saturation property. Although its standard deviation is not strictly the smallest, it achieves the smoothest spacing evolution, avoids severe oscillations, and offers the best overall trade-off among safety, stability, and response smoothness.

5.4 Comparison of distance-based and speed-based driving strategies

The previous analysis has shown that the APF control function provides balanced overall performance. However, in cooperative train operation, the control objective may still be defined with respect to different state variables. In the present study, two driving strategies are formulated within the APF framework: a distance-based driving strategy, which regulates train following directly through inter-train spacing, and a speed-based driving strategy, which regulates the following process through speed difference. The inter-train spacing histories under these two control objectives are compared in Figure 5.4, and the corresponding statistical results are listed in Table 5.3.

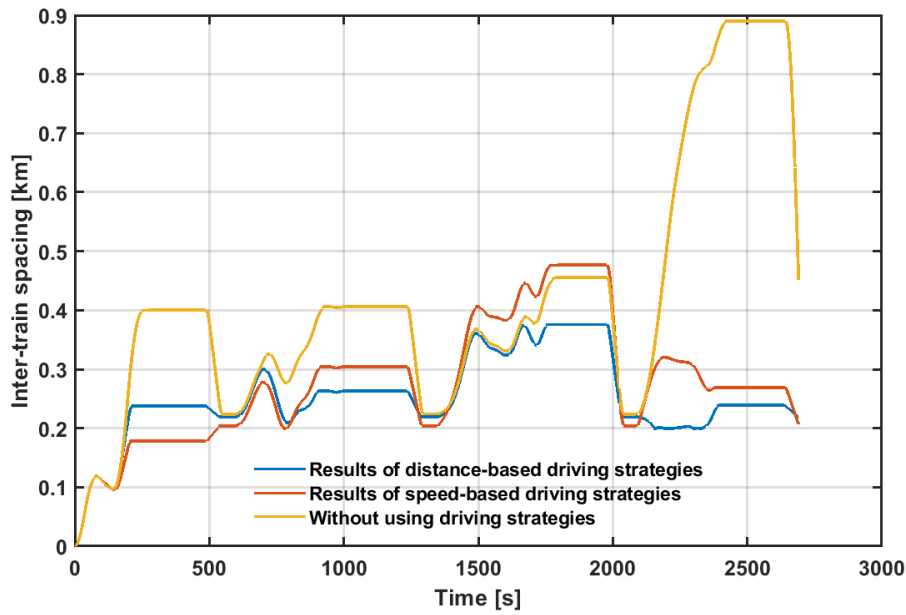


Figure 5.4 Inter-train spacing histories under distance-based and speed-based driving strategies

Table 5.3 Statistical comparison of inter-train spacing under distance-based and speed-based driving strategies

Control Mode	Mean (m)	Standard deviation (m)	Maximum (m)	Minimum (m)
Without driving strategies	418	212	895	226
Speed-based driving strategies	277	101	476	200
Distance-based driving strategies	252	69	379	200

As shown in Figure 5.4 and Table 5.3, the distance-based control exhibits overall smoother behavior. Its spacing history shows smaller fluctuations, with no notable oscillations even during acceleration or deceleration phases, and the corresponding standard deviation is lower. Its maximum spacing reaches only 379 m, smaller than the 476 m under the speed-based strategy, indicating stronger spacing maintenance. This difference fundamentally arises from the distinct sensitivity regions of the two strategies within the APF framework. When spacing approaches the target value, the distance-based strategy experiences a steeper APF gradient, allowing timely correction of small deviations and thus maintaining a stable following state. In contrast, the speed-

based strategy relies more heavily on speed differences. When the train speeds are similar, but the spacing remains large, the adjustment is triggered later, making local oscillations more likely during steady state operation.

Although the distance-based strategy performs better, its practical application in railway operation is subject to several limitations. First, absolute inter-train spacing typically relies on external measurement sources such as odometers, track circuits, or Global Navigation Satellite System (GNSS). These signals can be affected by track conditions, curve radius variation, gradient fluctuations, and other external interferences. In long-train operation and complex track environments, these effects may degrade the reliability of distance-based feedback. Second, distance-based control is generally more sensitive to information delay, because any lag in the transmitted or estimated position information directly affects the spacing calculation and may lead to delayed control action.

By contrast, speed-related information is generally easier to measure at high frequency and with good robustness using onboard sensors. Moreover, compared with absolute spacing, speed difference is less sensitive to cumulative positioning error and is therefore better suited to real-time control under rapidly changing operating conditions. For this reason, although the speed-based driving strategy does not produce the tightest spacing regulation in the present numerical comparison, it offers clear advantages in measurability, implementation robustness, and engineering feasibility.

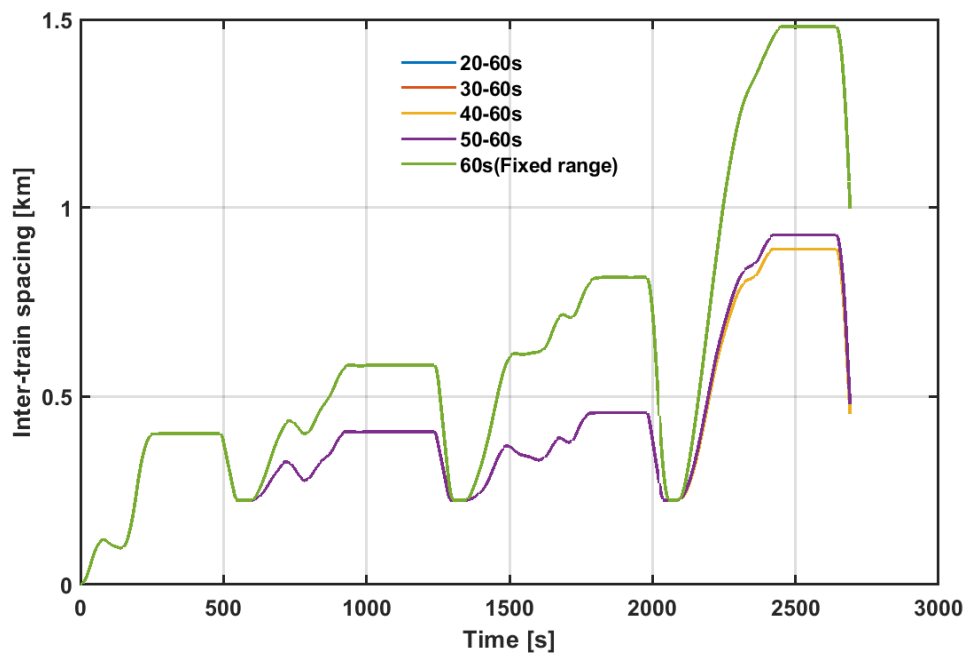
Overall, the comparison suggests that the choice of control objective has a clear influence on train-following behavior. If the emphasis is placed purely on compact spacing regulation, the distance-based strategy performs better. However, if practical factors such as information availability, robustness to measurement error, and suitability for real-time implementation are also taken into account, the speed-based driving strategy is more consistent with the engineering requirements of VC operation.

5.5 Optimization and sensitivity analysis of driving strategy parameters

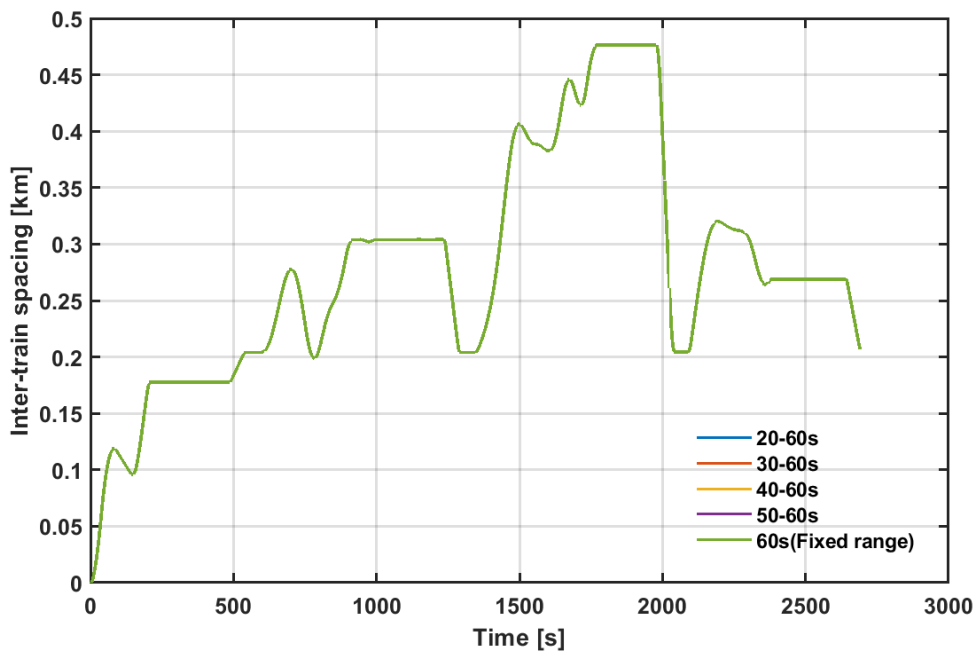
In practical operation, the performance of VC control depends not only on the adopted driving strategy but also on several critical parameters, such as start-up delay, acceleration constraints, and the initial inter-train spacing. These parameters determine how rapidly and to what extent the following train responds to changes in the motion of the leader train, and different parameter combinations may lead to distinct outcomes in terms of stability, speed, and safety margin. Therefore, a systematic sensitivity analysis of these key parameters is necessary to evaluate the robustness of the proposed driving strategy and its applicability under realistic engineering conditions.

5.5.1 Influence of start-delay settings

The start-delay is defined here as the time offset between the departure instant of the leader train and that of the following train after a stop or restart. It is an important external timing parameter affecting the following process in VC operation. In practice, this delay may arise from differences in dwell-time requirements, dispatching commands, signaling logic, and communication or processing delays. Different start-delay settings directly affect the departure timing of the following train and may therefore affect the inter-train spacing. The inter-train spacing histories under different start-delay settings are compared in Figure 5.5.



(a) Without driving strategy



(b) With driving strategy

Figure 5.5 Inter-train spacing histories under different start-delay settings

Here, “20–60 s” denotes that, according to the restart constrain, the minimum dwell time of the following train is set to 20s, while the maximum allowable dwell time is 60s. “30–60 s”, “40–60 s”, and “50–60 s” indicate that the minimum dwell time is adjusted to 30 s, 40 s, and 50 s, respectively, while the

maximum dwell time remains fixed at 60 s in all three cases. “60 s (Fixed range)” means that both the minimum and maximum dwell times are set to 60s, so the following train always departs after a fixed 60s stop.

As shown in Figure 5.5(a), although different start-delay settings are imposed, the inter-train spacing histories remain almost identical during the initial 0-600 s. During this stage, the two trains operate under similar track conditions, and the resulting traction and braking commands remain close. As a result, the influence of the start-delay has not yet accumulated sufficiently to produce visible differences in inter-train spacing. As the operation continues and the running conditions change, especially during pronounced acceleration or deceleration phases and when different control constraints become active, the effect of the start-delay gradually accumulates and begins to show differences in the spacing evolution.

In particular, when the minimum dwell time increases from 40 s to 60 s, the inter-train spacing grows markedly, reaching a maximum of approximately 1.4 km. This occurs because the following train remains stationary for a longer period, while the leader train continues to operate normally, quickly generating a substantial speed difference. After restarting, the following train adjusts its motion mainly according to track-related constraints, but without an active mechanism for compensating for the initial spacing increase caused by the delayed departure of the following train. Consequently, the early spacing deficit cannot be eliminated within a short time, and the discrepancy continues to accumulate during the subsequent run. This leads to a large long-term spacing and is unfavorable for cooperative operation.

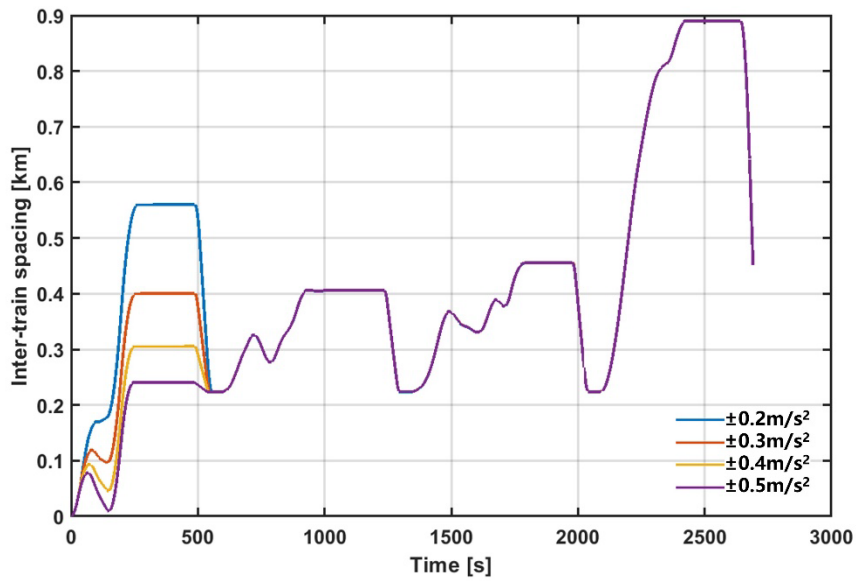
In contrast, after the driving strategy is introduced in Figure 5.5(b), the spacing histories under different start-delay settings coincide, and the inter-train spacing no longer changes with varying delay values. That is because when a larger start-delay produces an oversized spacing at departure, the attractive potential in the APF framework increases and drives the following train to accelerate. When the spacing becomes sufficiently small or the speed difference reverses, the repulsive term suppresses further pursuit and prevents the safety

spacing from being compressed. Through this mechanism, the spacing increase caused by the delayed departure of the following train can be corrected rapidly, so that the spacing trajectories under different delay settings converge to a similar following pattern.

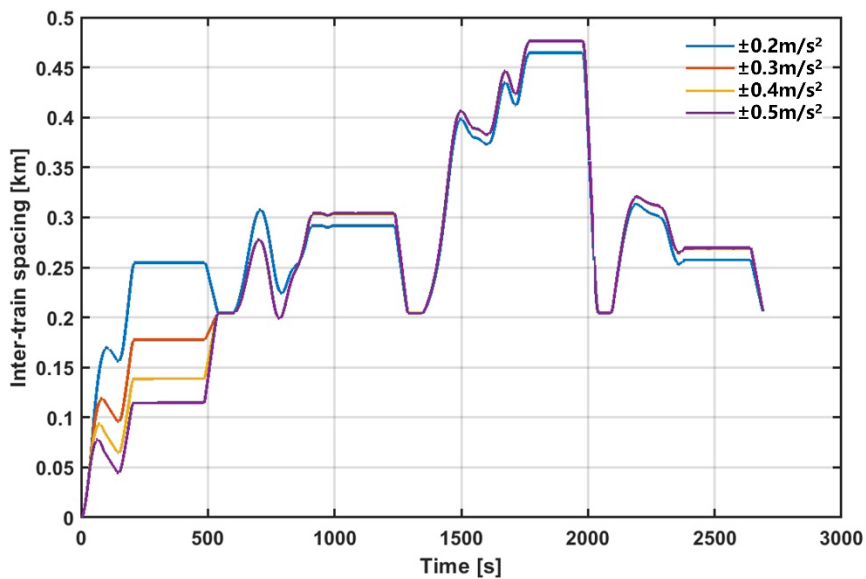
In real railway operation, start delays are often unavoidable and may vary over time. The fact that the driving strategy maintains stable following performance over a wide delay range of 20–60 s indicates that the system is robust to start-delay variations. This reduces the dependence on strictly synchronized departures and mitigates the operational risks caused by inconsistent platform operations or timing mismatch, thereby improving the practical feasibility of VC control in real-world applications.

5.5.2 Influence of acceleration limits

The acceleration limit is a key control constraint in longitudinal train operation and is jointly affected by traction capability, braking capability, and track conditions. Different upper bounds on allowable acceleration directly influence how quickly the following train can respond to changes in the motion of the leader train, thereby affecting the transient response and the long-term following performance of cooperative operation. To evaluate the influence of the acceleration limit on control performance, four representative limit level ($\pm 0.2 \text{ m/s}^2$, $\pm 0.3 \text{ m/s}^2$, $\pm 0.4 \text{ m/s}^2$, and $\pm 0.5 \text{ m/s}^2$) are considered, and the corresponding inter-train spacing histories are compared in Figure 5.6.



(a) Without driving strategy



(b) With driving strategy

Figure 5.6. Inter-train spacing histories under different acceleration limits

As shown in Figure 5.6(a), the influence of the acceleration limit is mainly concentrated in the initial 0–500 s interval. In this stage, a smaller acceleration limit weakens the ability of the following train to compensate for the speed difference created at departure. When the constraint is $\pm 0.2 \text{ m/s}^2$, the inter-

train spacing increases to about 0.56 km before 500 s. When the upper bound is increased to ± 0.3 , ± 0.4 , and ± 0.5 m/s², the maximum increased spacing in the start-up phase decreases progressively. This indicates that a larger available acceleration improves the catch-up capability of the following train and helps reduce the spacing more rapidly in the early stage.

However, after approximately 500 s, the four curves gradually converge and exhibit large oscillations in the 2000–2600s interval, with the maximum spacing reaching nearly 0.9 km. This behavior indicates that, without driving strategies, spacing variations in the later operation phases are mainly driven by external factors such as track gradient, curve radius, and speed restrictions, and the influence of the acceleration limits on stability is significantly reduced. Regardless of the available acceleration level, the system ultimately exhibits similar oscillation patterns and spacing divergence tendencies.

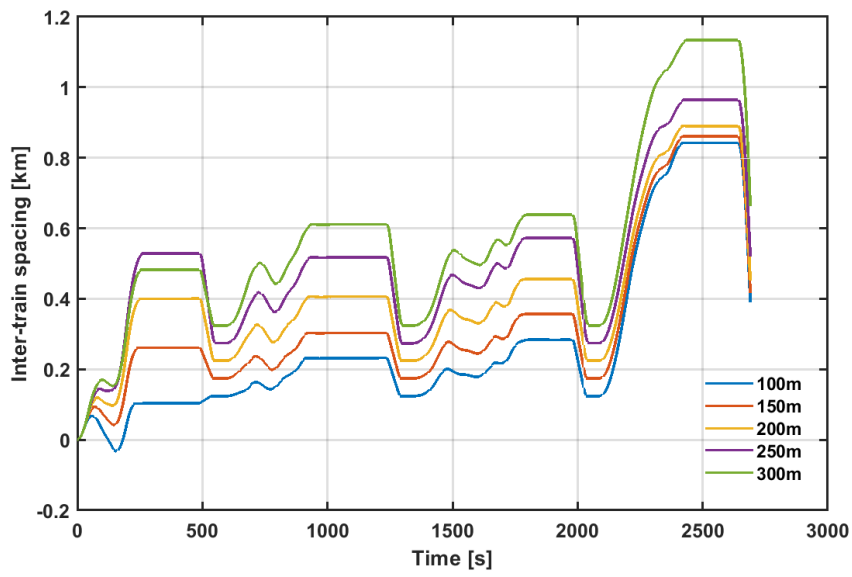
When the speed-based driving strategy is enabled, as shown in Figure 5.6(b), the inter-train spacing under different acceleration limits is significantly reduced, and the trajectories remain much closer than those in Figure 5.6(a), but the curves do not fully coincide. This indicates that the speed-based driving strategy suppresses the sensitivity to acceleration-limit settings, but does not eliminate it. In particular, during restart and re-acceleration phases, a larger acceleration limit still allows a stronger short-term response, so noticeable differences can remain in some parts.

From an engineering perspective, these results suggest that the acceleration limit mainly affects the transient adjustment capability of the following train. A larger limit improves short-term responsiveness, but may also increase the risk toward overshoot under complex operating conditions. After the speed-based driving strategy is introduced, the overall system becomes less sensitive to the exact value of the acceleration limit, although noticeable differences may still persist when stronger acceleration demand is required.

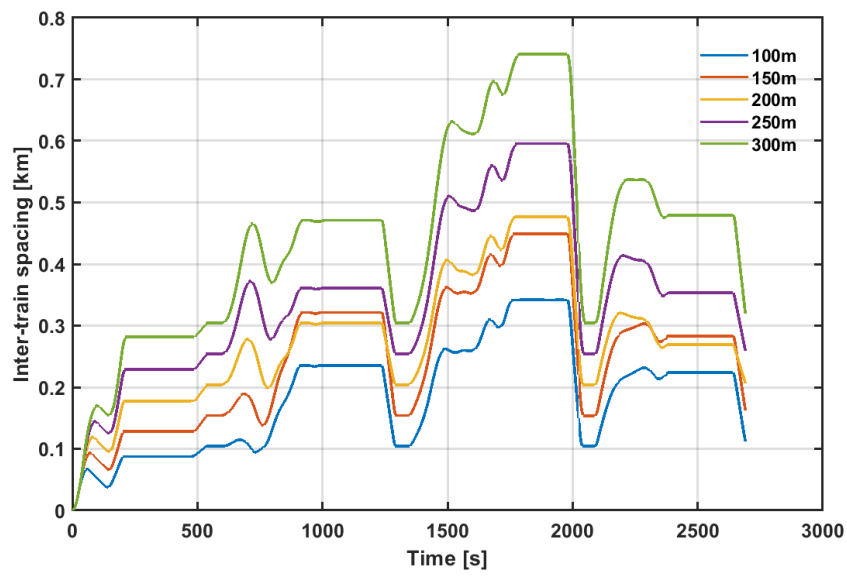
5.5.3 Effects of initial and target inter-train spacing settings

In VC train operation, the initial inter-train spacing and the target inter-train spacing describe two related but functionally different aspects of the following process. The initial inter-train spacing determines the starting condition when the following train enters the control domain and mainly affects the early transient adjustment, whereas the target inter-train spacing represents the desired spacing level that the controller aims to maintain during subsequent operation. In simple terms, the initial inter-train spacing specifies how far apart the two trains are when control begins, whereas the target inter-train spacing specifies how far apart the controller intends to keep them during stable following. Together, they influence the convergence of train following, the smoothness of spacing adjustment, and the overall safety margin of the system.

In the present tests, these two quantities are assigned the same prescribed value in each case (100, 150, 200, 250, and 300 m). Therefore, each tested spacing setting simultaneously defines both the starting spacing and the desired steady following spacing. The inter-train spacing histories under different prescribed spacing settings are compared in Figure 5.7, while the corresponding mean values and standard deviations are shown in Figure 5.8.

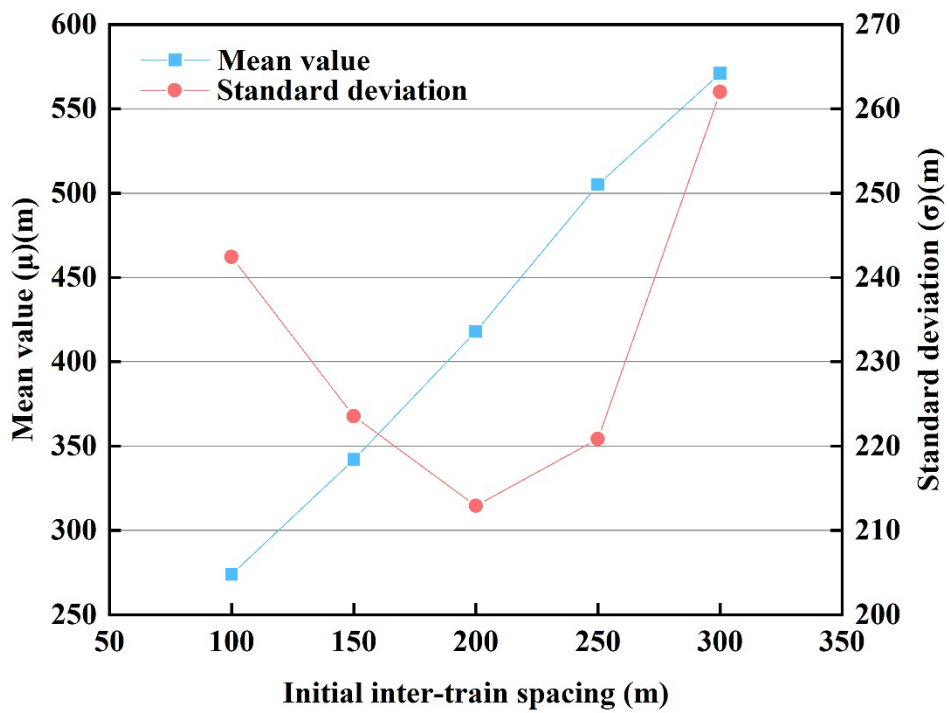


(a) Without driving strategies

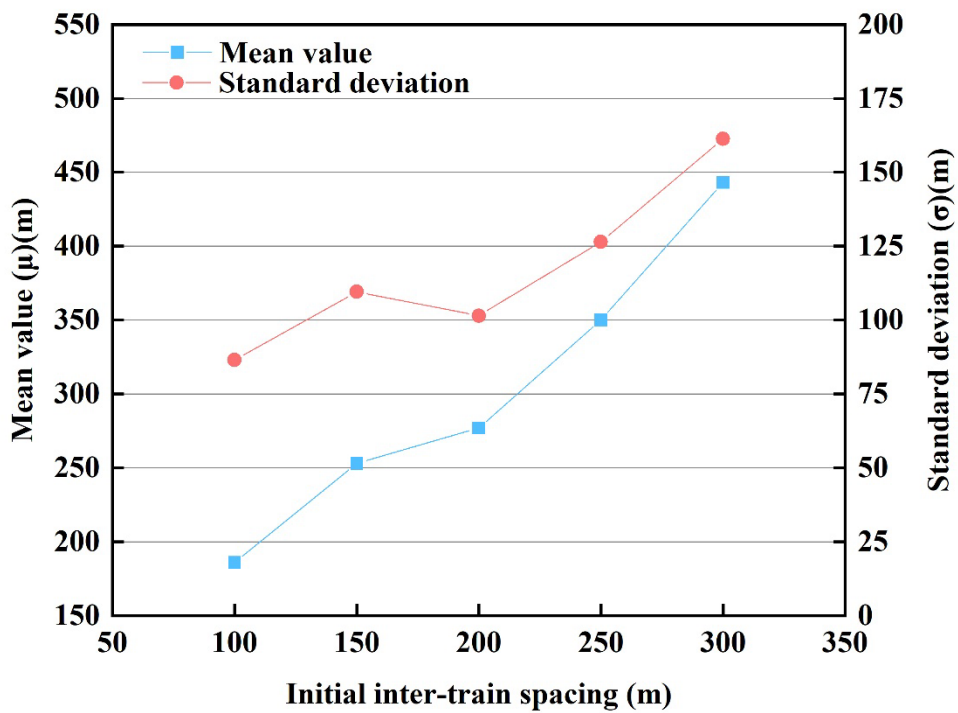


(b) With driving strategies

Figure 5.7 Inter-train spacing histories under different initial and target spacing



(a) Without driving strategies



(b) With driving strategies

Figure 5.8. Mean values and standard deviations under different initial and target spacing

As shown in Figure 5.7(a), when the prescribed spacing setting increases from 100 m to 300 m, the inter-train spacing histories shift upward as a whole, indicating that the system maintains a higher average spacing throughout the run. This is expected, because a larger prescribed spacing directly raises the desired operating level of the following process. At the same time, a larger initial spacing also means that the following train must reduce a larger early spacing deviation. However, its spacing-recovery capability is jointly limited by the acceleration upper bound, track gradient, and traction characteristics. Under a large prescribed spacing, the following train cannot fully reduce the spacing deviation within a limited time, even with continuous acceleration. Figure 5.8(a) further shows that the mean value increases monotonically with the prescribed spacing setting, whereas the standard deviation exhibits a U-shaped trend, with the minimum around 200 m, indicating the weakest spacing fluctuation and the best stability at this setting.

In contrast, when the speed-based driving strategy is enabled, as shown in Figure 5.7(b), the inter-train spacing histories under different prescribed spacing settings become much closer to one another, and the fluctuation level is clearly reduced compared with the case without strategy. This indicates that the influence of the initial spacing difference is largely absorbed by the control strategy during the following process. Figure 5.8(b) supports the same conclusion: although the mean value still increases with the prescribed spacing setting, both the mean level and the standard deviation are lower than those in Figure 5.8(a), indicating that the strategy reduces the sensitivity of the system to different spacing settings and maintains more consistent following behavior.

This improvement mainly results from the coordinated action of three mechanisms within the strategy. First, speed-based strategy continuously adjusts the motion of the following train according to the relative speed between the two trains, helping the system gradually reduce the spacing deviation. Second, the nonlinear APF structure strengthens the response when the spacing deviation is large, but weakens the control action naturally as the state approaches equilibrium, thereby improving convergence smoothness and avoiding excessive correction. Third, the predictive safety constraint limits the

control output when the spacing becomes too small or approaches the safety threshold, preventing excessive compression of the inter-train spacing. Through the combined effect of these mechanisms, the driving strategy exhibits strong self-regulation capability under different prescribed initial and target spacing settings, thereby maintaining stable and consistent train-following performance.

5.6 Summary

This chapter systematically evaluated the proposed cooperative control framework from the perspectives of model comparison, control-function formulation, control-objective selection, and parameter sensitivity. The results showed that the multi-point model provides a more physically consistent description of relative train motion than the single-point model, while the proposed driving strategy effectively suppresses inter-train spacing oscillations and improves following smoothness.

Among the compared control functions, the APF-based method showed the most balanced overall performance because of its smoother nonlinear regulation. In addition, although the distance-based driving strategy produced tighter spacing regulation in the present simulations, the speed-based driving strategy was found to be more suitable for practical implementation in view of measurability, real-time response, and engineering feasibility

Finally, the sensitivity analysis indicated that a start-delay range of 30–60 s, an acceleration upper bound of $\pm 0.3 \text{ m/s}^2$, and an initial/target inter-train spacing of around 200 m provide the most suitable overall parameter combination, achieving a good balance between response capability, running smoothness, and following stability.

6 Conclusions and future work

6.1 Conclusions

This study addresses the requirements of cooperative control for virtual coupling trains and develops a systematic driving strategy control framework. Through numerical simulations, the framework is evaluated from the perspectives of model formulation, control-function design, control-objective selection, and parameter sensitivity. The main conclusions are as follows:

(1) A cooperative train-following simulation framework for VC operation is established. By introducing the equivalent treatment of track geometry, the framework can incorporate gradients, curve radius, speed limits, and start-stop phases into a unified longitudinal modelling process, thereby providing a reliable basis for the analysis and evaluation of cooperative control strategies.

(2) A speed-based APF control function is proposed using speed difference together with the speed-integrated spacing-related variable, so that the control formulation no longer depends directly on absolute inter-train spacing as its primary input. Comparative analysis of different control functions shows that the APF-based formulation provides the most balanced overall performance under the present case settings, with smoother dynamic response, better suppression of spacing oscillations, and improved following stability.

(3) A cooperative control framework integrating the APF control function with predictive safety constraints is constructed. This framework combines the nonlinear regulation capability of the APF with the anticipatory effect of predictive safety control, achieving a better balance among responsiveness, robustness, and safety. Simulation results show that the proposed strategy can effectively reduce inter-train spacing fluctuations, limit unnecessary traction/braking switching, and maintain the trains within a safe following region under varying operating conditions.

(4) A systematic sensitivity analysis further identifies the applicable parameter ranges of the proposed strategy. Under the present simulation settings, a start-delay range of 30–60 s, an acceleration upper bound of ± 0.3 m/s², and an initial/target inter-train spacing of around 200 m provide the most suitable overall parameter combination, achieving a good balance between response capability, running smoothness, and following stability. These results provide quantitative guidance for practical parameter tuning.

In summary, the proposed modelling and control framework exhibits good coordination, stability, and engineering applicability under the considered VC scenarios, and provides a solid basis for further research and practical implementation.

6.2 Future work

Although this study establishes a modelling framework for cooperative control of VC trains and systematically evaluates the performance of multiple control strategies, there are still several limitations that deserve further investigation.

(1) The finite-horizon inter-train spacing prediction model in this study is based on a constant acceleration assumption, which limits prediction accuracy under complex operating conditions. Future work may incorporate more refined motion prediction models, including non-constant-acceleration models or data-driven prediction approaches, so as to better capture train dynamics.

(2) The present work focuses mainly on the cooperation between two trains and does not yet provide an in-depth analysis of overall coordination and control coupling in multi-train formations. Future studies may extend the framework to multi-train scenarios, investigating how control commands propagate along long train groups and how this affects overall operational safety.

(3) The validation in this study is primarily simulation-based and still lacks experimental support. Future work should include hardware-in-the-loop tests, virtual prototype validation, and line tests to further verify the proposed control strategies and assess their implementability and stability in real systems.

References

- [1] Bock, U., and J. Varchmin. "Enhancement of the occupancy of railroads using virtually coupled train formations." *World Congress on Railway Research (WCRR)*. 1999.
- [2] Braun, I., S. König, and Eckehard Schnieder. "Concepts on a future railway management system." *8th World Congress on Intelligent Transport Systems ITS America, ITS Australia, ERTICO (Intelligent Transport Systems and Services-Europe)*. 2001.
- [3] König, Stefan, and E. Schnieder. "Modeling and simulation of an operation concept for future rail traffic." *ITSC 2001. 2001 IEEE Intelligent Transportation Systems. Proceedings (Cat. No. 01TH8585)*. IEEE, 2001.
- [4] Henke, Christian, et al. "Organization and control of autonomous railway convoys." *Proceedings of the 9th International Symposium on Advanced Vehicle Control, Kobe, Japan*. Vol. 2. 2008.
- [5] Ständer, Dipl-Ing Tobias, Dipl-Ing Jörn Drewes, and Dipl-Wirtsch-Ing Imma Braun. "Operational and safety concepts for railway operation with virtual train-sets." *IFAC Proceedings Volumes* 39.12 (2006): 261-266.
- [6] Gkoumas, Konstantinos, et al. "Rail transport research and innovation in Europe: an assessment based on recent European Union projects." *Transportation Research Procedia* 72 (2023): 3633-3640.
- [7] Felez, Jesus, and Miguel Angel Vaquero-Serrano. "Virtual coupling in railways: A comprehensive review." *Machines* 11.5 (2023): 521.
- [8] Flammini, F., et al. "Towards Railway Virtual Coupling 2018 IEEE International Conference on Electrical Systems for Aircraft." *Railway, Ship*

Propulsion and Road Vehicles and International Transportation Electrification Conference, ESARS-ITEC. Vol. 9. 2018.

- [9] Di Meo, Carlo, et al. "ERTMS/ETCS virtual coupling: Proof of concept and numerical analysis." *IEEE transactions on intelligent transportation systems* 21.6 (2019): 2545-2556.
- [10] Tian, Huadong. Simulation Study of Train Tracking Operation Based on AnyLogic. MS thesis, Beijing Jiaotong University, 2021.
- [11] Jiang, Ming. "Comparative Analysis of Train Tracking Intervals between Moving Block and Quasi-Moving Block Systems." *Railway Communication and Signaling Engineering Technology*, vol. 14, no. 2, 2017, pp. 1–3.
- [12] Xin, Yajiang. "Study on Train Following Operation in Sections under Moving Block." *Railway Communication and Signaling*, no. 9, 2016, pp. 5–8.
- [13] Rail Transit Vehicle Interface Standards Committee of the IEEE Vehicular Technology Society. *IEEE Standard for Communications-Based Train Control (CBTC) Performance and Functional Requirements*. IEEE Std 1474.1-2004, Institute of Electrical and Electronics Engineers, 2005
- [14] Li, Jianxiong. *Research on Train Control Method of Virtual Coupling Oriented to Dynamic Coupling and Close Tracking*. Master dissertation, Beijing Jiaotong University, 2021.
- [15] Schumann, Tilo. "Increase of capacity on the shinkansen high-speed line using virtual coupling." *International Journal of Transport Development and Integration* 1.4 (2017): 666-676.
- [16] MOVINGRAIL. *Deliverables*. 2020, <https://movingrail.eu/public-information/deliverables>. Accessed 10 Jan. 2023.
- [17] Borges, Rafael Mendes, and Egidio Quaglietta. "Assessing hyperloop transport capacity under moving-block and virtual coupling operations." *IEEE Transactions on Intelligent Transportation Systems* 23.8 (2021): 12612-12621.
- [18] Liu, Yafei, et al. "An analytical optimal control approach for virtually coupled high-speed trains with local and string stability." *Transportation Research Part C: Emerging Technologies* 125 (2021): 102886.
- [19] Liu, Yafei, et al. "Distributed model predictive control strategy for constrained high-speed virtually coupled train set." *IEEE Transactions on Vehicular Technology* 71.1 (2021): 171-183.

- [20] Liu, Yafei, et al. "Control strategy for stable formation of high-speed virtually coupled trains with disturbances and delays." *Computer-Aided Civil and Infrastructure Engineering* 38.5 (2023): 621-639.
- [21] Zhao, Hui, et al. "Robust event-triggered model predictive control for multiple high-speed trains with switching topologies." *IEEE Transactions on Vehicular Technology* 69.5 (2020): 4700-4710.
- [22] Su, Shuai, et al. "A nonlinear safety equilibrium spacing-based model predictive control for virtually coupled train set over gradient terrains." *IEEE Transactions on transportation electrification* 8.2 (2021): 2810-2824.
- [23] Felez, Jesus, Yeojun Kim, and Francesco Borrelli. "A model predictive control approach for virtual coupling in railways." *IEEE Transactions on Intelligent Transportation Systems* 20.7 (2019): 2728-2739.
- [24] Mitchell, I. "ERTMS Level 4, Train Convoys or Virtual Coupling." *IRSE News*, 2016, <https://webinfo.uk/webdocssl/irse-kbase/ref-viewer.aspx?Refno=1882928268&document=ITC%20Report%2039%20Train%20convoys%20and%20virtual%20coupling.pdf>. Accessed 7 Oct. 2022.
- [25] Guanetti, Jacopo, Yeojun Kim, and Francesco Borrelli. "Control of connected and automated vehicles: State of the art and future challenges." *Annual reviews in control* 45 (2018): 18-40.
- [26] Zheng, Yang, et al. "Distributed model predictive control for heterogeneous vehicle platoons under unidirectional topologies." *IEEE Transactions on Control Systems Technology* 25.3 (2016): 899-910.
- [27] Vaquero-Serrano, Miguel A., and Jesus Felez. "A decentralized robust control approach for virtually coupled train sets." *Computer-Aided Civil and Infrastructure Engineering* 38.14 (2023): 1896-1915.
- [28] Felez, Jesus, Miguel Angel Vaquero-Serrano, and Juan de Dios Sanz. "A robust model predictive control for virtual coupling in train sets." *Actuators*. Vol. 11. No. 12. MDPI, 2022.
- [29] Yang, Yiming, and Fei Yan. "Research on train dynamic coupling strategy based on distributed model predictive control." *Journal of Physics: Conference Series*. Vol. 2183. No. 1. IOP Publishing, 2022.
- [30] Bai, Weiqi, et al. "Event-triggering communication based distributed coordinated control of multiple high-speed trains." *IEEE Transactions on Vehicular Technology* 70.9 (2021): 8556-8566.

- [31] Chu, Kai-ching. "Decentralized control of high-speed vehicular strings." *Transportation science* 8.4 (1974): 361-384.
- [32] Havaei, Pedram, and Mohammad Ali Sandidzadeh. "Intelligent-PID controller design for speed track in automatic train operation system with heuristic algorithms." *Journal of Rail Transport Planning & Management* 22 (2022): 100321.
- [33] Pickering, James E., Jason Davies, and Keith J. Burnham. "Development of model prototype to investigate closer running autonomous train operation: Seamless interchangeability." *2019 23rd International Conference on System Theory, Control and Computing (ICSTCC)*. IEEE, 2019.
- [34] Li, Shukai, et al. "Robust sampled-data cruise control scheduling of high speed train." *Transportation Research Part C: Emerging Technologies* 46 (2014): 274-283.
- [35] Qianqian, Zhao, and Wang Hongwei. "A multi-train cooperative control method of urban railway transportation based on artificial potential field." *2019 Chinese Automation Congress (CAC)*. IEEE, 2019.
- [36] Cao, Yuan, et al. "Parameter-varying artificial potential field control of virtual coupling system with nonlinear dynamics." *Fractals* 30.02 (2022): 2240099.
- [37] Gulzar, Muhammad Majid, et al. "Multi-agent cooperative control consensus: A comparative review." *Electronics* 7.2 (2018): 22.
- [38] Liu, Ling, et al. "Coordinated control method of virtually coupled train formation based on multi agent system." *International conference on smart vehicular technology, Transportation, Communication and applications*. Cham: Springer International Publishing, 2018.
- [39] Ling, L. I. U., et al. "Intelligent dispatching and coordinated control method at railway stations for virtually coupled train sets." *2019 IEEE Intelligent Transportation Systems Conference (ITSC)*. IEEE, 2019.
- [40] Wang, Xingguo, Deqing Huang, and Huanlai Xing. "A Train Cooperative Operation Optimization Method based on Improved Reinforcement Learning Algorithm." *2022 4th International Conference on Industrial Artificial Intelligence (IAI)*. IEEE, 2022.
- [41] Wang, Xingguo, et al. "A train cooperative operation optimization method considering passenger comfort based on reinforcement learning." *2022*

IEEE 11th Data Driven Control and Learning Systems Conference (DDCLS). IEEE, 2022.

- [42] Liu, Hongen, LuoJun Yang, and Hui Yang. "Cooperative optimal control of the following operation of high-speed trains." *IEEE Transactions on Intelligent Transportation Systems* 23.10 (2022): 17744-17755.
- [43] Jia, Yuqi, Deqing Huang, and Xuefang Li. "Tracking control of two virtually coupled trains via prescribed performance control method." *2022 IEEE 11th Data Driven Control and Learning Systems Conference (DDCLS)*. IEEE, 2022.
- [44] Geiberger, Philipp. "Monitoring energy efficiency of heavy haul freight trains with energy meter data." Master's thesis, *KTH Royal Institute of Technology*, 2021